BLINKING IN QUANTUM DOTS AND ENDOTHELIAL CELLS UNDER CURVATURE AND SHEAR STRESS

by

Mao Ye

A dissertation submitted to Johns Hopkins University in conformity with the requirements for the degree of Doctor of Philosophy of Physics and Astronomy

Baltimore, Maryland

November, 2014

Abstract

Two research topics at the interface of physics, materials science, and biology are presented in this dissertation, (1) blinking in quantum dots, and (2) endothelial cells under curvature and shear stress.

Quantum dot (QD) blinking is characterized by switching between an "on" and an "off" state, and power-law distributions of on and off times with exponents from 1.0 to 2.0. The origin of blinking behavior in QDs, however, has remained a mystery. We report an energy-band model for QDs that captures the full range of blinking behavior reported in the literature and provides new insight into features such as the gray state, power-law distributions of on and off times, and the power-law exponents.

The highly specialized endothelial cells in brain capillaries are a key component of the blood-brain barrier, forming a network of tight junctions that almost completely block paracellular transport. In contrast to vascular endothelial cells in other organs, we show that brain microvascular endothelial cells resist elongation in response to curvature and shear stress. Since the tight junction network is defined by endothelial cell morphology, these results suggest that there may be an evolutionary advantage to resisting elongation by minimizing the total length of cell-cell junctions per unit length of vessel.

BLINKING IN QUANTUM DOTS AND ENDOTHELIAL CELLS UNDER CURVATURE AND SHEAR STRESS

Approved by:

Dr. Peter C. Searson, Advisor
Department of Physics and Astronomy
Department of Materials Science and
Engineering
Johns Hopkins University

Dr. Sharon Gerecht
Department of Chemical and Biomolecular
Engineering
Johns Hopkins University

Dr. Daniel H. Reich
Department of Physics and Astronomy
Johns Hopkins University

Dr. Hai-Quan Mao
Department of Materials Science and
Engineering
Johns Hopkins University

Dr. Robert L. Leheny
Department of Physics and Astronomy
Johns Hopkins University

Acknowledgements

The completion of this dissertation is the milestone of my graduate study and I owe my gratitude to all who have helped me along the way.

My deepest gratitude goes to my advisor, Dr. Peter Searson. I have been very fortunate to have an advisor who is so supportive of and patient with students. He has always been there to talk to, provide suggestions, and give encouragement. I learned so much from him about the philosophy of research, the art of scientific writing, ways of communication, and giving presentations. I am deeply grateful to him.

A heartfelt acknowledgement goes out to my GBO and thesis committee which include Dr. Chia-Ling Chien, Dr. Collin Broholm, Dr. Benjamin Schafer, Dr. Tyrel McQueen, Dr. Sharon Gerecht, Dr. Hai-Quan Mao, Dr. Daniel Reich, and Dr. Robert Leheny. I thank their generosity on sharing time from their busy schedule to make my GBO and thesis defense happen.

I would like to thank Carm King, Priti Ramesh, Tabitha Brewster, Kelley Key, Marge Weaver, Jeanine Majewski, Dorothy Reagle, Sue Porterfield, Tracy Smith, Mary Spiro, Martin Rietveld, Gregg Nass, and Susana Rodriguez for their constant and warm assistance.

I sincerely thank Dr. Michael McCaffery and Erin Pryce for their training on immunostaining and confocal microscopy techniques at Integrated Imaging Center (IIC). I would like to thank Zhen Yang for being a close friend and collaborator. Her expertise in image processing has been an invaluable support to my research projects. I would like to thank Dr. Lian Guo, Dr. Janice Lin, Dr. Justin Galloway, Dr. Maya Zayats, Dr. Janice Lin, Dr. Fei Zhu, Dr. Pu Wang, Dr. Wei-Chien Hung, Dr. Wei-Chiang Chen, Andrew Wong, Yu-Ja Huang, Charli Dawidczyk, Amanda Levy, Chloe Kim, Adam Reinitz, Thomas Batcho, Stafford Enck, Ivan Kuznetsov, Henry Sanchez, Margot Hultz, and Hamsa Gowda for their help on my research projects. I also want to express my gratitude to other members of Searson Group, including Jeaho Park, Max Bogorad, Erin

To my friends and family

Table of Contents

List of Publications

1. **M. Ye**, and P. C. Searson, "Blinking in Quantum Dots: The Origin of the Grey State and Power Law Statistics", *Physical Review B*, **84**, 125317 (2011).

2. Z. Yang, J. A. Bogovic, A. Carass, **M. Ye**, P. C. Searson, and J. L. Prince, "Automatic Cell Segmentation in Fluorescence Images of Confluent Cell Monolayers Using Multi-Object Geometric Deformable Model", *Proceedings of SPIE*, **8669**, 866904, (2013).

3. A. D. Wong, **M. Ye**, A. F. Levy, J. D. Rothstein, D. E. Bergles, and P. C. Searson, "The Blood-Brain Barrier: An Engineering Perspective", *Frontiers in Neuroengineering*, **6**, 7 (2013).

4. **M. Ye**, H. M. Sanchez, M. Hultz, Z. Yang, M. Bogorad, A. D. Wong, and P. C. Searson, "Brain Microvascular Endothelial Cells Resist Elongation Due to Curvature and Shear Stress", *Scientific Reports*, **4**, 4681 (2014).

5. **M. Ye**, A. D. Wong, M. B. Ulmschneider, and P. C. Searson, "Quantitative Analysis of the Enhanced Permeation and Retention (EPR) Effect", *submitted*.

6. A. Reinitz, J. DeStefano, **M. Ye**, A. D. Wong, and P. C. Searson, "Brain Microvascular Endothelial Cells Resist Elongation Due to Shear Stress", *submitted*.

7. **M. Ye**, I. Kuznetsov, H. M. Sanchez, and P. C. Searson, "A Kinetic Model for Quantitative Analysis of Efflux Pump Transport in Resected Vessels", *in preparation*.

List of Tables

List of Figures

Chapter 1 Overview

This dissertation presents two research topics at the interface of physics, materials science, and biology. It is organized as follows: Chapter 1 will provide the overview; Chapter 2 will present the model implementation, results and discussion for blinking in quantum dots; Chapter 3 will present the methodology, results and discussion for the influence of curvature and shear stress on endothelial cells; Chapter 4 will summarize the two topics and provide future directions.

1.1 Blinking in Quantum Dots

Quantum dots (QDs) are semiconductor nanoparticles with diameter typically between 1 to 20 nm (Trindade, O'Brien et al. 2001). They have received considerable attention due to their size dependent properties (**Figure 1**) (Ekimov and Onushchenko 1981, Alivisatos 1996) and applications in fields such as solar cells (Huynh, Peng et al. 1999, Kramer and Sargent 2013), light emitting diodes (Mattoussi, Radzilowski et al. 1998), and biological imaging (Gao, Cui et al. 2004, Kairdolf, Smith et al. 2013). For biological imaging, quantum dots can be used to detect molecular biomarkers and tumor cells at high sensitivity and specificity when they are conjugated with biomolecular affinity ligands, such as antibodies, peptides, or small molecules (Lee, Na et al. 2003, Weissleder, Kelly et al. 2005, Liu, Cai et al. 2007). In single-molecule imaging, QDs exhibit on and off emission (blinking) when observed individually under a fluorescence microscope (Nirmal, Dabbousi et al. 1996). Blinking, also known as fluorescence intermittency, has been considered a mixed blessing in using QDs for single-molecule imaging as: (1) it results in loss of signal from the molecule being monitored; (2) it indicates the behavior of a single particle rather than aggregates (Kairdolf, Smith et al. 2013). For other technical

applications, blinking is a major obstacle when high yields of photon emission are desirable (Krauss and Peterson 2010).   Therefore, there has been strong motivation to understand, and even eliminate blinking of QDs since reported in 1996 (**Figure 2**) (Nirmal, Dabbousi et al. 1996).
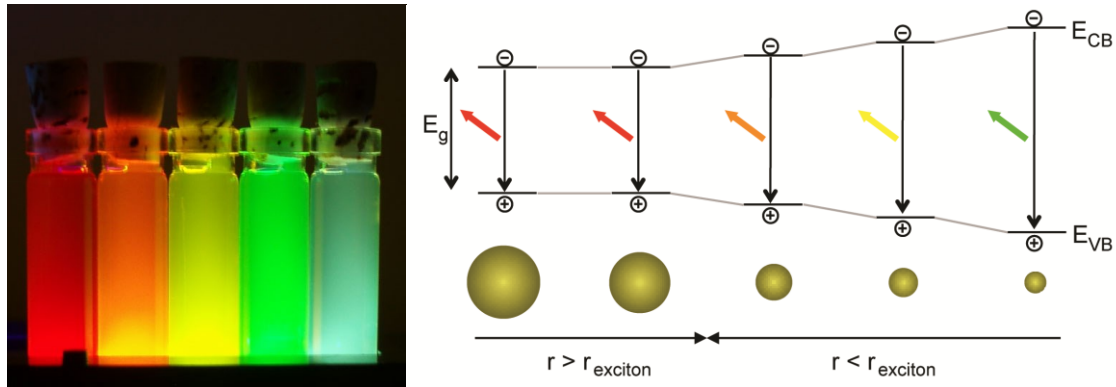
Figure 1.   Size-dependent photoluminescence colors of semiconductor QDs.

Left: QDs exhibit more blue color when diameter decreases.

Right: Band gaps of QDs increases when diameter decreases.
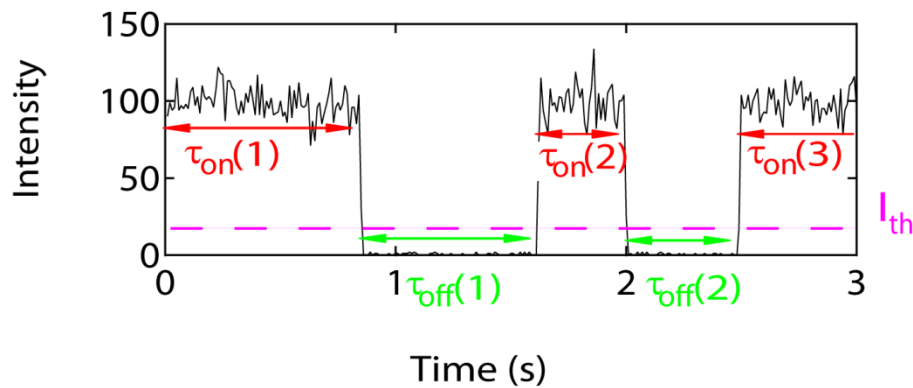
Figure 2.   Schematic illustration of fluorescence intermittency in quantum dots.

Typically a threshold is defined to separate the on and off intensities from intensity-time curves.

1.1.1 Quantum jumps in single ions

In 1915, Niels Bohr proposed his now famous model of an atom or molecule in which electrons occupy discrete energy levels (Bohr 1915, Frantsuzov, Kuno et al. 2008, Stefani, Hoogenboom et al. 2009). Although this model is not completely correct, it suggests the existence of energy levels (or orbits) of electrons and explains the Rydberg formula for the hydrogen atom

$$\frac{1}{\lambda_{vac}} = R\left(\frac{1}{n_1^2} - \frac{1}{n_2^2}\right)$$ **Equation 1**

where λ_{vac} is the wavelength of electromagnetic radiation emitted in vacuum, R is the Rydberg constant (approximately 1.097×10^7 m^{-1}), and n_1 (n_2) are integers ≥ 1 such that $n_1 < n_2$. The quantum jumps of electrons between discrete energy levels are often studied in samples containing a large number of atoms. Direct experimental observation of quantum jumps (fluorescence intermittency, or blinking) of a single atom (or ion) became feasible in the mid-1980s when individual ions could be trapped and addressed optically (Neuhauser, Hohenstatt et al. 1978, Nagourney, Janik et al. 1983, Cook and Kimble 1985).

A three-state model was proposed to explain the blinking in single ions, including ground state 0, excited state 1 with highly probable transition, and excited state 2 with much less frequent transition (Cook and Kimble 1985, Stefani, Hoogenboom et al. 2009). In this three-state model, an ion can absorb a photon and jump to excited state 1. After an emission of a photon, the ion can return to its ground state (**Figure 3**). Oscillation between ground state 0 and excited state 1 (strong transitions) will yield continuous stream of photons (on state). Occasionally, the ion may jump to excited state 2 with relatively longer de-excitation times (weak transitions) with no emitting photons (off state). Quantum jumps of weak transitions were claimed to be observed when switching between on and off states occurs. Exponential

distributions of on and off times were obtained experimentally, in perfect agreement with the prediction of "quantum jump theory" (Cook and Kimble 1985, Sauter, Neuhauser et al. 1986).
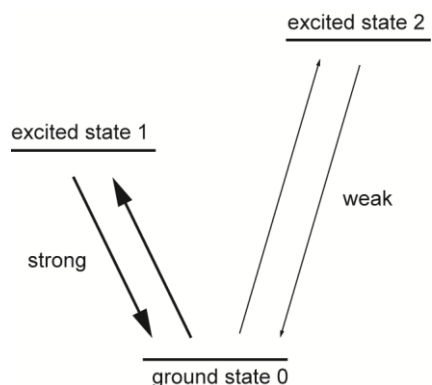
Figure 3. Energy levels for single-ion fluorescence intermittency experiment.

1.1.2 Blinking features in quantum dots

The breakthrough of single-molecule detection led to observations of blinking in various other fluorophores since the early 1990s, including semiconductor quantum dots (Nirmal, Dabbousi et al. 1996, Kuno, Fromm et al. 2000, Neuhauser, Shimizu et al. 2000, Kuno, Fromm et al. 2001, Shimizu, Neuhauser et al. 2001, Schlegel, Bohnenberger et al. 2002, Fisher, Eisler et al. 2003, Chung and Bawendi 2004, Pelton, Grier et al. 2004, Zhang, Chang et al. 2006), nanorods (Wang, Querner et al. 2006, Knappenberger, Wong et al. 2008, Roy, Aguirre et al. 2011), nanowires (Protasenko, Hull et al. 2005, Glennon, Tang et al. 2007, Protasenko, Gordeyev et al. 2007), single molecules (Haase, Hübner et al. 2004, Hoogenboom, van Dijk et al. 2005, Yeow, Melnikov et al. 2006, Hoogenboom, Hernando et al. 2007, Wustholz, Bott et al. 2007), fluorescent proteins (Dickson, Cubitt et al. 1997), and polymer segments (Bout, Yip et al. 1997).

In 1996, Nirmal et al. reported for the first time of blinking in individual quantum dots (Nirmal, Dabbousi et al. 1996). Individual CdSe QDs were embedded in a thin polyvinylbutyral film at room temperature, and fluorescence intensity-time curves were recorded under continuous illumination. The distributions of on and off times for four different samples were "strongly non-exponential", as opposed to the prediction of exponential distributions by the "quantum jump theory". It was soon discovered by Kuno et al. that the distributions of on and off times can be described by power-laws (Kuno, Fromm et al. 2000). The power-law behavior ($f = B\tau^{-\alpha}$) extends over 5 orders of magnitudes in time (< 1 ms to > 100 s) with exponents (α) between 1.5 and 1.7. Later on, various experiments were performed on studying the blinking behavior of quantum dots. Several key facts are summarized as follows: (1) the power-law exponents (α) are mostly found between 1.0 and 2.0 (Cichos, von Borczyskowski et al. 2007, Frantsuzov, Kuno et al. 2008, Krauss and Peterson 2010), (2) on and off time are generally uncorrelated, or at most weakly uncorrelated (Fernando, Xinhua et al. 2005), (3) off intensities can be significantly above the background (gray state) (Gómez, van Embden et al. 2009, Spinicelli, Buil et al. 2009), and (4) photoluminescence decay appears to be much faster for quantum dots with multiple carriers compared to single *e-h* pair (Klimov, Mikhailovsky et al. 2000, Jha and Guyot-Sionnest 2009).

1.1.3 Theoretical models on blinking in quantum dots

In 1997, Efros and Rosen (Efros and Rosen 1997) proposed the most cited model for QD blinking (**Figure 4**). In this four state model based on semiconductor physics, a QD (state 1) can absorb a photon generating an electron-hole pair (state 2). Radiative band-to-band recombination results in emission of a photon (and return to state 1), whereas absorption of a

second photon, before recombination of the electron-hole pair, leads to the creation of two electron-hole pairs (state 3). There are two possible pathways from this state: (1) radiative band-to-band recombination (return to state 2), and (2) non-radiative Auger recombination with simultaneous excitation of an electron to a trap state, resulting in a valence band hole and a trapped electron (state 4). The trapped electron is assumed to have very slow detrapping kinetics resulting in the off state. Auger recombination is an intra-QD energy transfer interaction in which the excess energy from a band-to-band recombination event is transferred to a spectator charge carrier rather than emitted as a photon. Efros-Rosen model provided an intuitive picture for blinking based on semiconductor physics; however, it is inconsistent with the "non-exponential" distributions of on and off times for blinking in quantum dots.
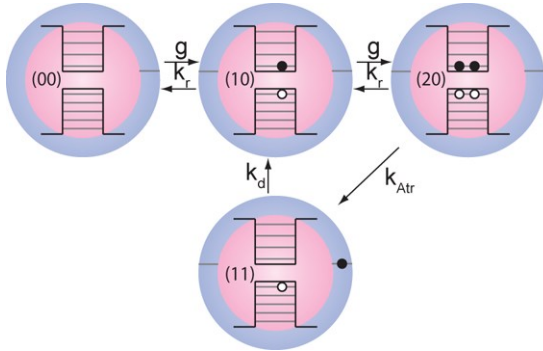
Figure 4. Energy-band diagrams for the Efros & Rosen Model.

g - generation rate, k_r - recombination rate constant, k_{Atr} - Auger-assisted trapping rate constant, k_d - detrapping rate constant. Absorption of a photon results in the generation of an electron-hole pair ($n = 1$ and $p = 1$). Radiative band-to-band recombination returns the system to the initial state with the emission of a photon. When there are more than 2 electron-hole pairs, Auger-assisted trapping will operate in parallel with radiative recombination. The on state is recovered only by detrapping. While this model can generate intensity-time curves similar to experimental data, it cannot explain features such as the power law distribution of on and off times, the gray state, or the generation of multiple electron-hole pairs.

Various modifications to the Efros-Rosen model have been suggested to explain the power-law behavior (Frantsuzov, Kuno et al. 2008).   They include the following:

Fluctuating barrier model.   Kuno et al. (Kuno, Fromm et al. 2003) suggested a model where the fluctuations in the height or width of a tunneling barrier between an electron and an external trap state leads to varying trapping and detrapping rates (**Figure 5a**).   Power-law distributions of on and off times were obtained.

Spectral diffusion model.   Shimizu et al. (Shimizu, Neuhauser et al. 2001) hypothesized a resonant tunneling mechanism where diffusion of acceptor energy levels in phase space (**Figure 5b**) leads to varying trapping and detrapping rates.   Tau and Marcus (Tang and Marcus 2005) further developed this model and obtained power-law distributions of on and off times.

Multiple-trap model.   Verberk et al. (Verberk, van Oijen et al. 2002) assumed a static distribution of trapping and detrapping rates, owing to the existence of multiple electron traps near the quantum dot (**Figure 5c**), and obtained power-law distributions of off times.   The probability density to tunnel at distance r from the quantum dot surface is assumed to be $p(r) = ae^{-ar}$, and the detrapping rate is assumed to vary exponentially with distance e^{-br}.   The power-law exponent (α) is equal to $1 + a/b$.

Spatial diffusion model.   Margolin et al. (Margolin and Barkai 2004) suggested a 3D diffusion in space of an ejected electron before its return (**Figure 5d**).   This model predicts the power-law exponent (α) to be 1.5, and deviations from 1.5 results from anomalous diffusion processes.

Fluctuating detrapping model.   Frantsuzov and Marcus (Frantsuzov and Marcus 2005) suggested a model where the fluctuations of detrapping (**Figure 5e**) lead to power-law distributions of on and off times with exponent 1.5.
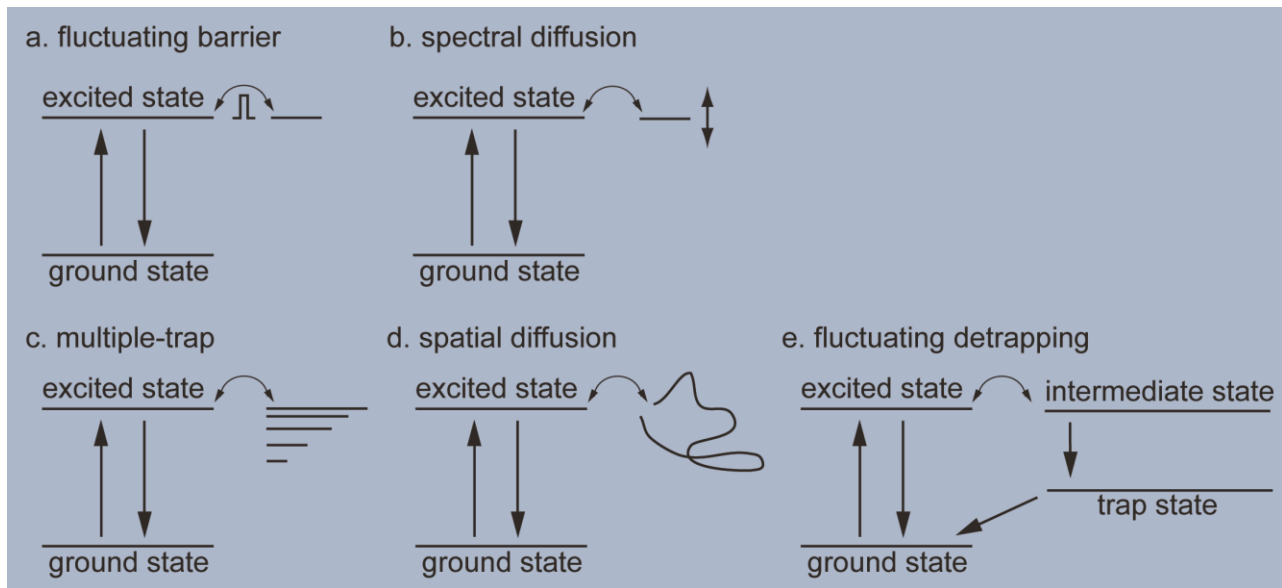
Figure 5. Schematic diagrams of various blinking models.

(a) Fluctuating barrier model: the tunneling barrier varies during the electron jumps.

(b) Spectral diffusion model: the electron jumps to/from the trap when it is in resonance with the excited state.

(c) Multiple trap model: the electron jumps between excited state and one of the multiple traps.

(d) Spatial diffusion model: the electron diffuses around in 3D space and returns.

(e) Fluctuating detrapping model: The non-radiative recombination rate of the excited state varies.

While these models provided useful insight into the power-law behavior by varying the on-to-off and off-to-on rates, the physics of the blinking behavior remains unresolved (Verberk, van Oijen et al. 2002, Kuno, Fromm et al. 2003, Margolin and Barkai 2004, Frantsuzov, Kuno et al. 2008).

1.2 Endothelial Cells under Curvature and Shear Stress

The diameter of blood vessels in humans ranges from about 8 μm in capillaries to more than 1 cm in large elastic arteries, a range of more than four orders of magnitude (Aird 2005). In

larger vessels there are hundreds of cells around the perimeter, whereas in a capillary a single endothelial cell may wrap around to form a junction with itself as well as its upstream and downstream neighbors (Reese and Karnovsky 1967, Brightman 1977, Abbott, Ronnback et al. 2006, Daneman 2012, Wong, Ye et al. 2013).

1.2.1 Structure and function of the blood-brain barrier

The blood brain barrier (BBB) is the interface between the vascular system and the brain. Historically, the blood brain barrier has been defined by the layer of endothelial cells that form the vessel/capillary walls.   More recently, the concept of the neurovascular unit has been introduced to recognize that brain health depends on functional interactions between neurons and non-neuronal cells such as vascular cells (endothelial cells and pericytes) and glia (astrocytes, microglia, and oligodendroglia; **Figure 6**) (Hawkins and Davis 2005, Abbott, Patabendige et al. 2010, Wong, Ye et al. 2013).   This is a highly dynamic system in which cells transduce biochemical and biomechanical signals in complex microenvironments involving basement membrane and extracellular matrix.   These non-neuronal cells are responsible for the physical, biochemical, and immune barriers of the central nervous system (CNS) that regulate the microenvironment of neurons which is key for signal transduction, remodeling, angiogenesis, and neurogenesis (Wong, Ye et al. 2013).
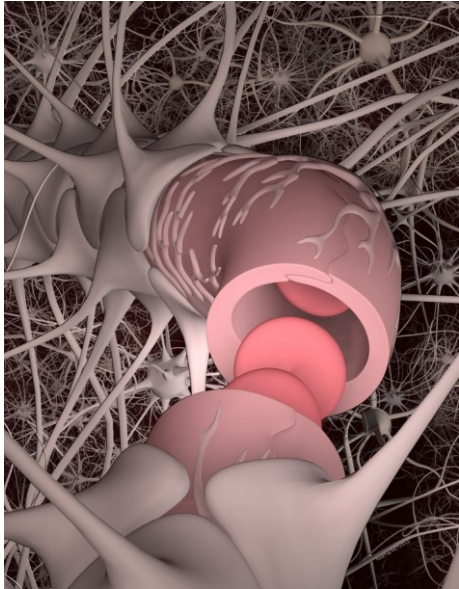
Figure 6.   The neurovascular unit of the blood-brain barrier.

The microvascular endothelial cells that form the lumen of brain capillary are partially covered by pericytes and basement membrane, and almost completely surrounded by the end feet of astrocytes.   Functional interactions between BMECs, astrocytes, pericytes, other glial cells, and neurons are key to regulating brain homeostasis.

The endothelial cells that line the microvasculature in the brain define the interface between the vascular system and the brain.   These cells function as adaptive non-linear input/output devices where input from biochemical and biomechanical forces in the local microenvironment of the neurovascular unit influences cell phenotype as manifested by cell morphology, protein expression, gene expression, proliferation, transport, etc (Dejana 2004, Aird 2005, Aird 2007, Aird 2007).   In addition to biochemical and biomechanical input from the vascular system, numerous paracrine signaling pathways between microvascular endothelial cells, astrocytes and pericytes are responsible for maintenance of the blood-brain barrier (Aird 2007, Aird 2007, Abbott, Patabendige et al. 2010).

In the brain microvasculature, cell-cell junctions are key to maintaining the integrity of the brain microvasculature and regulating paracellular transport.   Cell-cell adhesion is achieved

through the formation of adherens junctions and tight junctions (Bazzoni and Dejana 2004, Dejana 2004, Aird 2007). Both adherens junctions and tight junctions involve homophilic interactions between the extracellular domains of membrane proteins and are linked to the actin cytoskeleton via intracellular partners. Endothelial adherens junctions are formed by the extracellular domains of vascular endothelial cadherin (VE-cadherin) and are linked to the actin cytoskeleton inside the cell via proteins such as α-catenin, β-catenin, and vinculin (Bazzoni and Dejana 2004, Dejana 2004). The tight junctions in the brain microvasculature prevent paracellular transport of most molecules and severely restrict transport of small ions. Therefore, transcellular transport is responsible for most molecular trafficking between the vascular system and the brain. Various methods for transient disruption of tight junctions have been explored for drug delivery, and local disruption of tight junctions is associated with many diseases of the central nervous system. Tight junctions are formed between claudins (Nitta, Hata et al. 2003), although other proteins such as occludin are also present (Hawkins and Davis 2005, Furuse and Tsukita 2006). These tight junction membrane proteins are connected to the actin cytoskeleton via zona occludin (ZO) adaptor molecules (ZO-1 and ZO-2) (Hawkins and Davis 2005).

It is responsible for maintaining the homeostasis of the brain by regulating the chemical environment, immune cell transport, and entry of xenobiotics. The concentrations of water, ions, amino acids, hormones, and neurotransmitters in the blood undergo fluctuations, particularly after eating or exercise. If such fluctuations were allowed to occur in the brain it would lead to local disruption of signal propagation and uncontrolled neural activity. Therefore, transport from the capillary lumen to the brain parenchyma must be tightly regulated.

The morphology of microvascular endothelial cells is dependent in part on biomechanical input from the vascular system. Key studies of the influence of curvature and shear stress on endothelial cells are summarized below.

1.2.2 Studies of endothelial cells under curvature

Curvature is a fundamental physical property that influences a wide range of everyday processes. For endothelial cells in vessels (**Figure 7**), if curvature is energetically unfavorable, then its effects can be minimized by elongating along the length of the vessel to avoid wrapping around in the radial direction. Conversely, if curvature is energetically favorable then cells may elongate in the radial direction to wrap around the vessel and contract in the axial direction (**Figure 8**). Since tight junctions in brain capillaries are responsible for preventing paracellular transport, we hypothesize that cell morphology may play an important role in the structure and function of the blood-brain barrier.
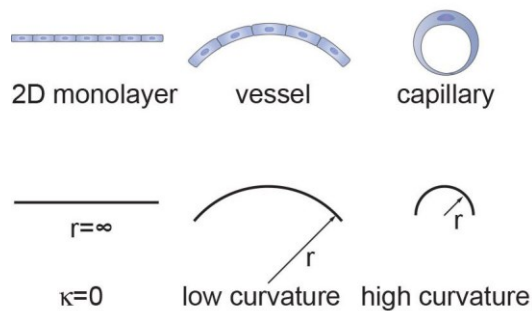
Figure 7. Curvature in confluent monolayers of endothelial cells.

In 2D monolayers the curvature is zero. In large vessels the curvature is relatively low. In capillaries, cells may wrap around to form tight junctions with themselves as well as their neighbors. The small capillary diameter results in high curvature.
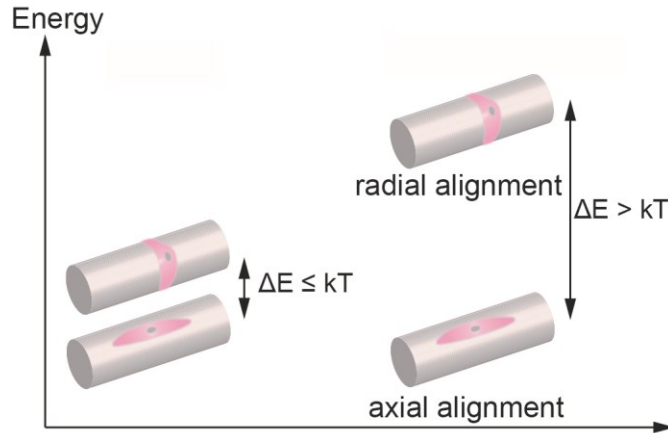
Figure 8. Schematic illustration showing different energy states for axial and radial alignment.

We consider the energy associated with axial and radial alignment of an endothelial cell on a cylindrical surface. When the energy difference (ΔE) between the two states (axial and radial) is less than the thermal energy (kT, where k is the Boltzmann constant and T is temperature), there is no driving force for preferential alignment. In contrast, when the energy for radial orientation is larger than for axial alignment, radial alignment is energetically unfavorable.

Previous studies of the influence of curvature on cell behavior have focused on the motility of isolated cells in the context of tumor cell invasion (Curtis and Varde 1964, Dunn and Heath 1976, Nerem, Levesque et al. 1981, Rovensky and Samoilov 1994, Svitkina, Rovensky et al. 1995, Levina, Domnina et al. 1996). Isolated fibroblasts seeded on small diameter glass rods (< 200 μm) were shown to exhibit preferential elongation and alignment (Curtis and Varde 1964, Dunn and Heath 1976, Fisher and Tickle 1981), and preferential migration along the cylinder axis, leading to the concept of contact guidance as a possible mechanism for tumor cell invasion. These studies suggest that curvature may play a role in regulating the morphology and function of endothelial cells in confluent monolayers.

1.2.3 Studies of endothelial cells under shear stress

13

Blood pressure exerts a force normal to a vessel wall that imposes a circumferential stress on the vessel, whereas blood flow results in a frictional drag, or shear stress, parallel to the endothelium in the direction of blood flow (**Figure 9**).   These stresses play an important role in regulating endothelial cell morphology and function, and in mediating a wide range of signaling and transport processes between the vascular system and surrounding tissue (Chien 2007, Hahn and Schwartz 2009, Johnson, Mather et al. 2011, Daniel and Martin 2012).   These stresses are also thought to play an important role in regulation of the blood-brain barrier (Krizanac-Bengez, Mayberg et al. 2004, Neuwelt, Abbott et al. 2008, Tarbell 2010, Cucullo, Hossain et al. 2011, Neuwelt, Bauer et al. 2011).

For an ideal Newtonian fluid (incompressible), the shear stress τ in a straight cylindrical vessel under constant laminar flow is given by the Poiseuille equation: $\tau = 4\mu Q/\pi r^3$ where μ is the dynamic viscosity, Q is the volumetric flow rate, and r is the radius of the lumen.   Therefore, the magnitude of the shear stress on the endothelium is proportional to the flow rate and viscosity, and inversely proportional to r^3.   Consequently, endothelial cells in vessels with high flow rate and small diameter are exposed to large shear stress.

The viscosity of blood is about 4 cP (0.004 Pa·s), significantly larger than the viscosity of water of 0.7 cP (0.0007 Pa·s) at 37°C, primarily due to the presence of red blood cells.   Typical time averaged values of shear stress are $4 - 30$ dynes cm^{-2} in the arterial circulation and $1 - 4$ dynes cm^{-2} in the venous circulation (Turitto 1982, Kamiya, Bukhari et al. 1984, Papaioannou and Stefanadis 2005, Koutsiaris, Tachmitzi et al. 2007, Dolan, Kolega et al. 2013).   The flow rate in capillaries is typically from 6 to 12 nL min^{-1} corresponding to a shear stress of $10 - 20$ dynes cm^{-2} for a capillary 10 μm in diameter (taking $\mu = 1$ cP or 0.001 Pa s) (Kamiya, Bukhari et al. 1984).
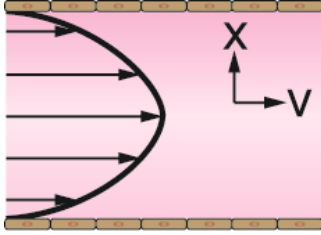
Figure 9. Flow velocity profile of blood flow in axial cross-section of a blood vessel.

While the influence of curvature has been relatively unexplored, the role of shear stress on endothelial cell morphology and function has been more widely studied. Endothelial cells in blood vessels in sections away from branch points show elongation and axial alignment (Reidy and Lowell Langille 1980, Nerem, Levesque et al. 1981). In cell culture, a physiological shear stress results in a transition from a cobblestone-like morphology to an elongated spindle-like morphology and alignment in the direction of flow (Eskin, Ives et al. 1984, Levesque and Nerem 1985, Davies 1995, Malek and Izumo 1996, Simmers, Pryor et al. 2007), very similar to the morphology observed in large resected vessels.

Chapter 2 Blinking in Quantum Dots

In this chapter, I will describe our energy-band model for QDs that captures the range of blinking behavior reported in the literature and provides insight into features such as the gray state, the power-law distribution of on and off times, and the power-law exponents.

2.1 Model Implementation

2.1.1 Intensity-time curves

Figure 10 shows energy-band diagrams for the various states in our model, along with the associated rate constants. Our model is implemented using standard kinetic Monte Carlo methods (KMC) (Fichthorn and Weinberg 1991) and is based on the physics of QDs (Brus 1986, Nozik, Beard et al. 2010) combined with descriptions for recombination and trapping processes widely used in device physics (**Table 1**). We denote each state in the QD as (*ij*), where *i* is the total number of free electrons (holes) in the QD, and *j* is the number of trapped charge carriers. Without loss of generality, we assume that only electrons can be trapped. From examination of **Figure 10** it is evident that $p = i$, $n = i - j$, and $s^- = j$, where *n* is the number of free electrons, *p* is the number of holes, and s^- is the number of occupied trap states.
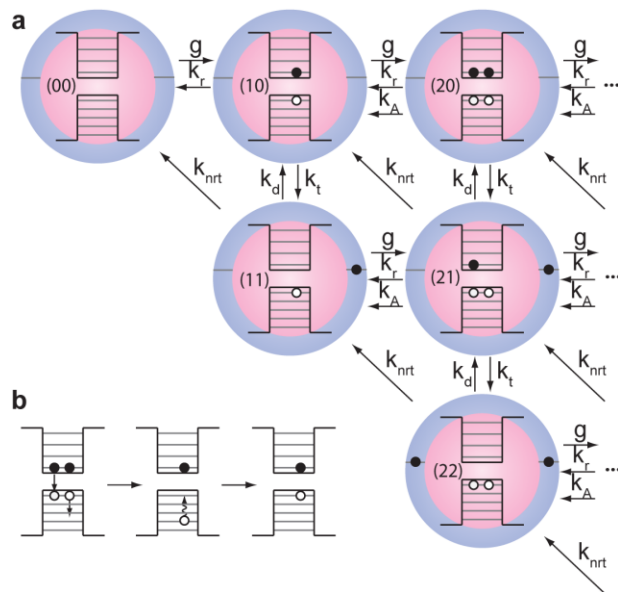
Figure 10. Energy band diagrams illustrating the dynamics of electron-hole pairs in blinking quantum dots.

(a) Physical processes in quantum dot blinking. g - generation rate, k_r - recombination rate constant, k_A - rate constant for Auger recombination, k_t - trapping rate constant, k_d - detrapping rate constant, k_{nrt} - rate constant for non-radiative recombination.

(b) Auger recombination in quantum dots. Band-to-band recombination is coupled with excitation of a charge carrier (in this case a hole) that quickly relaxes (on the order of picoseconds) back to the band edge.

17

Process	Rate equation	
Radiative recombination	$r_r = k_r np$	k_r: rate constant for radiative recombination
		n: number of electrons
		p: number of holes
Auger recombination	$r_A = k_A np^2$	k_A: rate constant for Auger recombination
Trapping		k_t: rate constant for trapping
		s: total number of trap states ($s = s^0 + s^-$)
		s^-: number of occupied trap states
		Note: we arbitrarily choose $s = s^0 + s^- = 10$
Detrapping	$r_d = k_d s^-$	k_d: rate constant for detrapping
Nonradiative recombination		k_{nrt}: rate constant for nonradiative recombination

Table 1. Summary of processes included in the model and the corresponding rate equations.

For each state (*ij*) there are several possible transitions to adjacent states, and these transitions have corresponding rates r_1, r_2, … r_n. The time that a QD will remain in a certain state is given by $\Delta t = -\ln R / \sum r_i$, where R is a random number between 0 and 1. The probability that a QD will move to a particular state is given by $r_i / \sum r_i$. A QD with no electrons or holes is designated as in the (00) state ($n = 0$, $p = 0$, $s^- = 0$). Absorption of a photon and the generation of an *e-h* pair results in a transition to the (10) state ($n = 1$, $p = 1$, $s^- = 0$). From the (10) state, there are three possible transitions, indicated by the arrows in **Figure 10**: (1) radiative recombination (k_r) returns the QD to the (00) state with the emission of a photon, (2) trapping of the electron (k_t) results in a transition to the (11) state ($n = 0$, $p = 1$, $s^- = 1$), and (3) absorption of another photon (g) results in a transition to the (20) state ($n = 2$, $p = 2$, $s^- = 0$).

The transition from the (10) state is determined from the sum of all possible rates ($r_r + r_t + g$), as described above. For the (10) state, the residence time is given by $\Delta t = -\ln R/(r_r + r_t + g)$. We then subdivide the range from 0 to 1 into three parts, each with a length the same as the probability of each transition. For example, the probability of the transition from the (10) state to the (00) state is determined by $r_r/(r_r + r_t + g)$. The transition is then selected by generating another random number between 0 and 1. Since k_r is typically much larger than g and k_t, there is a high probability that the QD will relax from the (10) state to the (00) state. Oscillation between the (00) and (10) states represents sequential absorption and emission in the QD. Population of the (20) state gives rise to the possibility of Auger recombination, which is usually considered to be faster than radiative recombination. For all transitions between (i0) states, the QD is considered to be in the on state and no blinking is observed. Even though Auger recombination (k_A) may dominate in (i0) states with $i \geq 2$, we consider these configurations as on states as they return to the (00) state with high probability.

The population of states with trapped carriers ($j \geq 1$) results in off states. For example, consider the (21) state ($n = 1$, $p = 2$, $s^- = 1$) for which there are six possible transitions: (1) return to the (20) state by detrapping (k_d), (2) transition to the (10) state by non-radiative recombination involving the trap state (k_{nrt}), (3) transition to the (31) state by absorption of a photon and generation of an e-h pair (g), (4) transition to the (11) state by radiative recombination and generation of a photon (k_r), (5) transition to the (11) state by Auger recombination (k_A), and (6) transition to the (22) state by trapping the conduction band electron (k_t).

From **Figure 10** it is evident that if $k_A > k_r$ (and $k_A > k_t$, k_d, k_{nrt}) then the QD will remain in the off state since e-h pair generation will most likely be followed by a return to the same state through non-radiative Auger recombination (k_A). Detrapping (k_d) and non-radiative

recombination via trap states (k_{nrt}) both return the QD to the on state.   Switching between the on and off states that leads to blinking is controlled by k_t, k_d, and k_{nrt} which are generally much slower than g, k_r, and k_A.   The intensity-time curves are obtained by counting the number of photons emitted in each bin (integration) time (I_n).

2.1.2 On-time fraction

To characterize the blinking behavior for a given set of rate constants, we first write the system of rate equations corresponding to the processes indicated in **Figure 10**.   We denote the probability of finding a QD in a given state by P_{ij}.   For example, the (00) state can be accessed from the (10) state by radiative recombination (k_r), or from the (11) state by non-radiative recombination via trap states (k_{nrt}).   In addition, the (00) state can transition to the (11) state by generation of an *e-h* pair (g) which would decrease the probability of finding a QD in the (00) state.   Thus, the time dependent probability for the (00) state is given by:

$$\frac{dP_{00}}{dt} = k_r P_{10} + k_{nrt} P_{11} - g P_{00} \quad \textbf{Equation 2}$$

As an example, the system of equations for a maximum of 2 *e-h* pairs is

$$\frac{dP_{00}}{dt} = k_r P_{10} + k_{nrt} P_{11} - g P_{00} \quad \textbf{Equation 3}$$

$$\frac{dP_{10}}{dt} = g P_{00} + k_d P_{11} + 1 \cdot 2 k_{nrt} P_{21} + (2 \cdot 2 k_r + 2 \cdot 2^2 k_A) P_{20} - (k_r + s k_t + g) P_{10} \quad \textbf{Equation 4}$$

$$\frac{dP_{20}}{dt} = g P_{10} + k_d P_{21} - (2 \cdot 2 k_r + 2 \cdot 2^2 k_A + 2 s k_t) P_{20} \quad \textbf{Equation 5}$$

$$\frac{dP_{11}}{dt} = s k_t P_{10} + 2 \cdot 2 k_{nrt} P_{22} + (1 \cdot 2 k_r + 1 \cdot 2^2 k_A) P_{21} - (k_d + k_{nrt} + g) P_{11} \quad \textbf{Equation 6}$$

$$\frac{dP_{21}}{dt} = 2 s k_t P_{20} + g P_{11} + 2 k_d P_{22} - [k_d + 2 k_{nrt} + 2 k_r + 1 \cdot 2^2 k_A + 1 \cdot (s-1) k_t] P_{21} \quad \textbf{Equation 7}$$

$$\frac{dP_{22}}{dt} = 1 \cdot (s-1) k_t P_{21} - (2 \cdot 2 k_{nrt} + 2 k_d) P_{22} \quad \textbf{Equation 8}$$

The equations can be solved for different values of the rate constants by recognizing that in steady state $dP_{ij}/dt = 0$ and that $\sum P_{ij} = 1$. The on-time fraction P_{on} is given by

$$P_{on} = \sum P_{i0} \quad \textbf{Equation 9}$$

The off-time fraction P_{off} is given by

$$P_{off} = \sum_{j \geq 1} P_{ij} \quad \textbf{Equation 10}$$

Experimentally, P_{on} is usually obtained by defining a threshold (I_{th}) between the on and off intensities (I_{on} and I_{off}). This procedure may introduce artifacts; however, as long as the on and off intensities are well separated then P_{on} is the same for both methods.

2.1.3 Computing distributions of on and off times

Intensity distributions were obtained from intensity-time curves. To obtain the on and off times, we first determined the threshold intensity I_{th} from the intensity distribution. Gaussians were fit to the on and off peaks and I_{th} was obtained from intersection point between the two peaks. The QD was considered to be "on" when $I_n \geq I_{th}$, and "off" when $I_n < I_{th}$. If I_n remains above or below I_{th} for n sequential time bins, then $\tau_{i,on/off} = i\tau_{bin}$. The intensity-time curve is thus converted to a sequence of on and off times. We then create a histogram describing the number of occurrences N_i of each duration τ_i ($1 \leq i \leq M$). The shortest duration (τ_1) is limited by the bin time (τ_{bin}), while the longest duration (τ_M) is limited by the total time (τ_{total}). Total number of occurrences of on or off times is

$$N^{total} = \sum_{1 \leq i \leq M} N_i \quad \textbf{Equation 11}$$

The distribution of on and off times, or formally, the probability density f_i, is given by

$$f_i = \frac{N_i / N^{total}}{[(\tau_{i+1} - \tau_i) + (\tau_i - \tau_{i-1})]/2} \quad \textbf{Equation 12}$$

where $2 \leq i \leq M - 1$. At the limits ($i = 1$ and $i = M$) we set $\tau_0 = \tau_1$ and $\tau_{M+1} = \tau_M$. The power-law exponents ($\alpha_{on/off}$) or exponential times ($\tau_{0,on/off}$) are determined from a least-squares fit of the $\log(f_{i,on/off})$ versus $\log(\tau_{i,on/off})$ curves.

2.1.4 Quantum yield

The on and off quantum yields were calculated by averaging all the intensities above or below the threshold over time divided by the number of photogenerated electron-hole pairs:

$$QY_{on} = \frac{\sum_{I_n \geq I_{th}} I_n}{\sum g_n} \quad \textbf{Equation 13}$$

$$QY_{off} = \frac{\sum_{I_n < I_{th}} I_n}{\sum g_n} \quad \textbf{Equation 14}$$

Experimentally, evaluation of QY_{on} and QY_{off} requires careful analysis of the distribution of intensities from intensity-time curves. If the intensities associated with the on and off states are well separated then it is trivial to set an appropriate threshold. However, if the distributions of on and off intensities overlap, then distinguishing between on and off states is more difficult. This can often be accomplished by fitting two Gaussians to the distribution, one representing the on state and one representing the off state.

2.1.5 Generation

The generation rate g (ms^{-1}) in a spherical QD with absorption coefficient α (cm^{-1}) is given by:

$$g = \frac{I_0 \pi d^2}{4 h \upsilon} \left[1 - 2 \frac{1 - (1 + \alpha d) e^{-\alpha d}}{(\alpha d)^2} \right] \quad \textbf{Equation 15}$$

where I_0 is the incident power density (W cm^{-2}), $h\nu$ is the photon energy, and d is the QD diameter.   We assume that the absorption coefficient for a nanoparticle is the same as for a bulk material.

Absorption can also be defined in terms of the absorption cross-section σ.

$$\sigma = \frac{\pi d^2}{4}\left[1 - 2\frac{1-(1+\alpha d)e^{-\alpha d}}{(\alpha d)^2}\right]$$ **Equation 16**

such that $g = I_0\sigma/h\nu$.

For a 5 nm diameter CdSe QD, taking an absorption coefficient $\alpha = 10^5$ cm^{-1} at $\lambda = 400$ nm (Gupta and Doh 1992) and an incident power density of $0.1 - 1000$ W cm^{-2} (Peterson and Nesbitt 2008, Goushi, Yamada et al. 2009, Spinicelli, Buil et al. 2009) the generation rate g is typically in the range $1 - 10^4$ ms^{-1}.

The generation rate is linearly dependent on incident power density, QD volume, and absorption coefficient (**Figure 11**).   The bulk absorption coefficient for most semiconductors of interest is in the range from $10^5 - 10^6$ cm^{-1}.   The QD diameter is typically $3 - 10$ nm, corresponding to an order of magnitude range of volume.   Although the range of power density may be quite large, experimentally, the power density is adjusted so that the emission from the QD does not saturate the detector using an exposure time of around 10 ms.
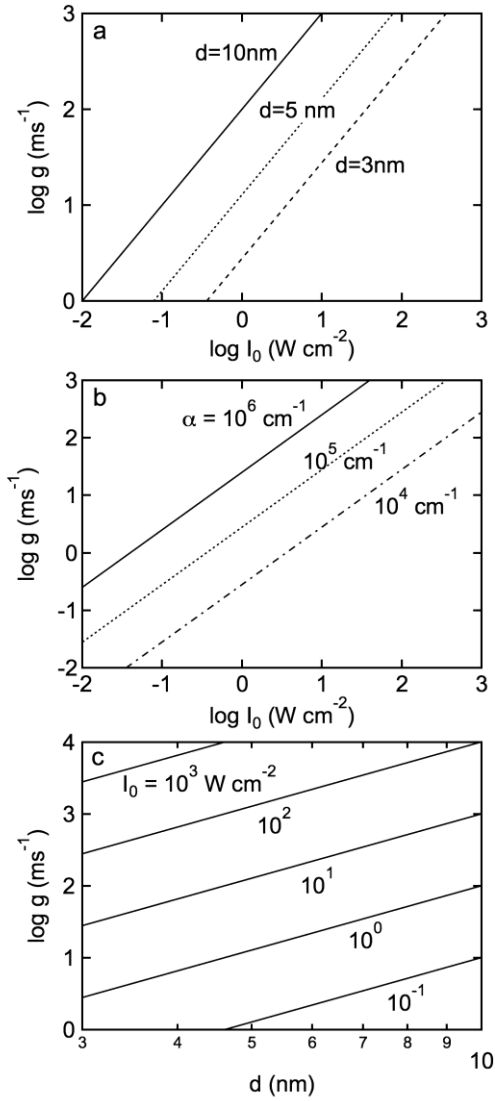
Figure 11. The dependence of generation rate on different parameters.

(a) Generation rate versus incident power density for d = 3, 5, and 10 nm taking $\alpha = 10^5$ cm^{-1} at λ = 400 nm. (b) Generation rate versus incident power density for $\alpha = 10^6$ cm^{-1}, 10^5 cm^{-1}, and 10^4 cm^{-1} taking d = 3 nm. (c) Generation rate versus QD diameter for incident power densities of 0.1, 1, 10, 100, and 1000 W cm^{-2} taking $\alpha = 10^5$ cm^{-1} at λ = 400 nm.

2.1.6 Trapping and detrapping

Radiative band-to-band recombination is expected to be fast with a rate constant $k_r = 10^3 -$

10^6 ms^{-1} (**Table 2**) (Landsberg 1970, Michler, Imamoglu et al. 2000, Crooker, Hollingsworth et

al. 2002, Fomenko and Nesbitt 2007, Mahler, Spinicelli et al. 2008, Wang, Ren et al. 2009). If there are more than two free carriers in a QD, Auger recombination (**Figure 10b**) is expected to be dominant with a rate constant $k_A = 10^5 - 10^8$ ms^{-1} (Haug 1983, Klimov, Mikhailovsky et al. 2000, Wang, Califano et al. 2003, Kraus, Lagoudakis et al. 2005, Jha and Guyot-Sionnest 2009). For convenience we refer to the different configurations in **Figure 10** as (*ij*) where *i* represents the number of *e-h* pairs and *j* represents the number of trapped electrons.

Parameter	Typical values (ms^{-1})
k_r	$10^3 - 10^6$
k_A	$10^5 - 10^8$
g	$1 - 10^3$
Constant trapping and detrapping rates	
k_t	$10^{-4} - 10^2$
$k_d + k_{nrt}$	$10^{-3} - 10^{-2}$
Variable trapping and detrapping rates	
k_t	$10^{-2} - 10^2$
$k_d + k_{nrt}$	$10^{-5} - 10^{-1}$
$r_{t,\text{eff}}$	$10^{-5} - 10^{-1}$
$r_{d,\text{eff}}$	$10^{-5} - 10^{-1}$

Table 2.   Typical values of parameters used in the energy-band model.

It is evident from examination of an energy-band diagram (**Figure 10**) that trapping, detrapping and Auger recombination are essential to create configurations where blinking is observed. In configurations where trap states are occupied ($j \geq 1$), electron - hole pairs are

eliminated primarily by Auger recombination ($k_A > k_r$) and the QD is predominantly in an off state. Conversely, configurations where $j = 0$ can easily reach the (10) state where radiative recombination dominates. Thus configurations in the top row ($j = 0$) represent the on state of a QD, and configurations below the top row ($j \geq 1$) correspond to the off state.

The rate of trapping is given by $r_t = k_t n s^0$ where n is the number of electrons in the QD and s^0 is the number of empty trap states. The detrapping rate is given by $r_d = k_d s^-$ where s^- is the number of occupied trap states. For all results reported here, we arbitrarily choose 10 trap states ($s = 10$), although as we show later, the steady state number of trapped electrons is typically < 3.

Blinking requires switching between an on state ($i0$) and an off state (ij) where $j \geq 1$. The overall trapping and detrapping rates for a single QD, taking into account all configurations, can be described in terms of effective trapping and detrapping rates:

$$r_{t,\text{eff}} = \frac{\sum r_{t,i0} P_{i0}}{\sum P_{i0}} = \frac{s k_t \sum P_{i0}}{\sum P_{i0}} \quad \textbf{Equation 17}$$

$$r_{d,\text{eff}} = \frac{\sum (r_{d,i1} + r_{nrt,i1}) P_{i1}}{\sum_{j \geq 1} P_{ij}} = \frac{k_d \sum P_{i1} + k_{nrt} \sum i P_{i1}}{\sum_{j \geq 1} P_{ij}} \quad \textbf{Equation 18}$$

Where P_{ij} is the probability of state (ij). The blinking behavior can then be described in terms of the on-time fraction P_{on}, as a function of $r_{t,\text{eff}}$ and $r_{d,\text{eff}}$:

$$P_{\text{on}} = \frac{r_{d,\text{eff}}}{r_{t,\text{eff}} + r_{d,\text{eff}}} \quad \textbf{Equation 19}$$

where $P_{\text{on}} = 1$ for a QD that is always on and $P_{\text{on}} < 1$ for blinking. To achieve the on and off times observed experimentally, typically in the range from 1 ms to 100 s, the effective trapping and detrapping rates should be on the order of $10^{-5} - 10^0$ ms^{-1}.

2.2 Results and Discussion

Intensity-time curves from the model are able to reproduce the full range of behavior observed experimentally. **Figure 12a** shows a typical non-blinking luminescence curve. For an integration (bin) time of 10 ms, the distribution of on intensities shows a peak at around 100 photons, corresponding to a quantum yield of 1.0. Increasing $r_{t,\mathrm{eff}}/r_{d,\mathrm{eff}}$ to 10^{-1} by changing k_t, results in blinking with $P_{\mathrm{on}} = 0.91$ (**Figure 12b**). The average on intensity (I_{on}) remains 100 photons per bin ($QY_{\mathrm{on}} = 1.0$) with a maximum frequency of 91% of the value for the corresponding non-blinking curve (**Figure 12a**). The off-intensity distribution is much narrower than the on-intensity distribution, and would only be observed experimentally if the fluctuations are larger than the noise of the photodetector. Increasing $r_{t,\mathrm{eff}}/r_{d,\mathrm{eff}}$ to 10^0 decreases P_{on} to 0.5 (**Figure 12c**), and increasing $r_{t,\mathrm{eff}}/r_{d,\mathrm{eff}}$ further to 10^1, decreases P_{on} to 0.09 (**Figure 12d**). These results show that the blinking behavior is controlled by $r_{t,\mathrm{eff}}/r_{d,\mathrm{eff}}$.

Figure 12e shows that the blinking regime occurs over a range of $r_{t,\mathrm{eff}}/r_{d,\mathrm{eff}}$ from 10^{-2} to 10^2. To illustrate the relative importance of the parameters in the model, we consider a simple case involving the (00), (10), (11), (21) states. These are the four states most frequently occupied at low generation rates. Taking into account the relevant rate constants, it is straightforward to show that:

$$r_{t,\mathrm{eff}} = \frac{sk_t g}{g + k_r} \quad \textbf{Equation 20}$$

$$r_{d,\mathrm{eff}} = \frac{(k_d + k_{nrt})(k_r + 2k_A)}{g + k_r + 2k_A} \quad \textbf{Equation 21}$$

In most cases of experimental interest, $k_r > g$ and hence $r_{t,\mathrm{eff}} \to sk_t g/k_r$. Similarly, it is also expected that $k_r + 2k_A > g$, so that $r_{d,\mathrm{eff}} \to k_d + k_{nrt}$ and hence P_{on} is independent of k_A (at constant

s, k_t, and $k_d + k_{nrt}$).   Deviations from these approximations are observed at higher generation rates.
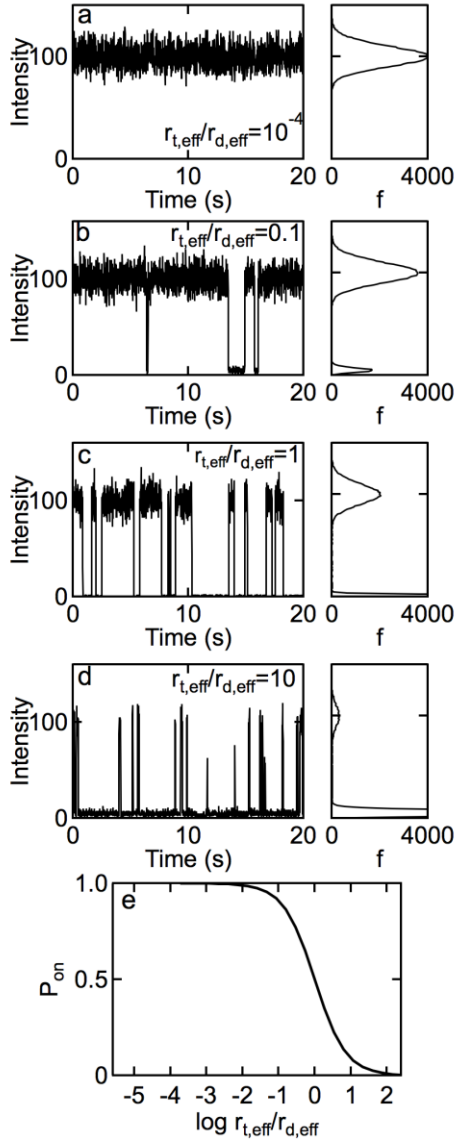
Figure 12.   Simulated intensity-time curves, and intensity distributions as a function of effective trapping/detrapping ratio $r_{t,\text{eff}}/r_{d,\text{eff}}$.

Here $k_d = 10^{-3}$ ms^{-1}, $k_{nrt} = 0$ ms^{-1}, $s = 10$, $k_r = 10^5$ ms^{-1}, $k_A = 10^7$ ms^{-1}, $g = 10$ ms^{-1}.   (a) $r_{t,\text{eff}}/r_{d,\text{eff}} = 10^{-4}$ ($k_t = 10^{-4}$ ms^{-1}), (b) $r_{t,\text{eff}}/r_{d,\text{eff}} = 10^{-1}$ ($k_t = 10^{-1}$ ms^{-1}), (c) $r_{t,\text{eff}}/r_{d,\text{eff}} = 10^0$ ($k_t = 10^0$ ms^{-1}), and (d) $r_{t,\text{eff}}/r_{d,\text{eff}} = 10$ ($k_t = 10$ ms^{-1}).   In all cases the integration (bin) time was 10 ms.   (e)

Dependence of P_{on} on the effective trapping/detrapping ratio $r_{t,eff}/r_{d,eff}$ showing that blinking occurs over a range of $r_{t,eff}/r_{d,eff}$ from 10^{-2} to 10^{2}.

From **Equation 19** it is seen that increasing the generation rate results in an increase in $r_{t,eff}$ and hence is expected to decrease P_{on}.   The generation rate is dependent on several parameters, however, for a given system it is very difficult to vary the generation rate over a wide range: the generation rate must be high enough so that the signal on the detector allows the on and off states to be clearly distinguished, but not too high to result in saturation.

The trapping and detrapping processes are controlled by k_t and $k_d + k_{nrt}$. k_t and k_d can be described by two possible mechanisms (Shockley and Read 1952).   (1) Trapping and detrapping involve delocalized electrons and states at the core/shell interface.   Energetically, the trap states are expected to be located in the band gap so that trapping is downhill and detrapping is thermally activated.   (2) Trapping and detrapping occur by tunneling between delocalized electrons in the core to states in the shell or at the surface of the shell if it is sufficiently thin. Non-radiative recombination via trap states k_{nrt} contributes to blinking in the same way as k_d even though they represent different physical processes.   The expressions for k_t, k_d and k_{nrt} are dependent on the mechanism but do not influence the results reported here.

2.2.1 Binning time and total time

The binning time, which is usually set by the minimum camera exposure time necessary to distinguish the QD from the background (typically in the range from 200 μs to 100 ms, but usually around 10 ms) (Kuno, Fromm et al. 2001, Peterson and Nesbitt 2008, Crouch, Sauter et al. 2010), plays a key role in determining the blinking characteristics.   If the effective trapping and detrapping rates, $r_{t,eff}$ and $r_{d,eff}$ are faster than $1/\tau_{bin}$, then switching is likely to occur in each frame and the QD will appear always on with an average intensity $I_{av} = I_{max} \cdot P_{on}$, where $I_{max} =$

$g \tau_{\text{bin}}$.   Conversely, if $r_{t,\text{eff}}$ and $r_{d,\text{eff}}$ are slower than $1/\tau_{\text{total}}$ (where τ_{total} is typically up to 1000 s), then there will be very few switching events in intensity-time curves.   Thus for blinking to occur, $r_{t,\text{eff}}$ and $r_{d,\text{eff}}$ must be $> 1/\tau_{\text{bin}}$ and $< 1/\tau_{\text{total}}$.   Practically, this corresponds to a range from about 10 ms to $\sim$ 100 s.

2.2.2 Gray state

Experimentally, intensity-time curves for QDs sometimes show an off-state that is above the background signal of the detector, the so-called gray state (Jha and Guyot-Sionnest 2009, Spinicelli, Buil et al. 2009, Zhao, Nair et al. 2010).   **Figure 13a** shows an intensity-time curve where the parameters are the same as for **Figure 12c** except that k_A is decreased from 10^7 ms^{-1} to 10^6 ms^{-1}.   The intensity distribution (**Figure 13a**) shows the emergence of a gray state where the off-state distribution is shifted above zero.
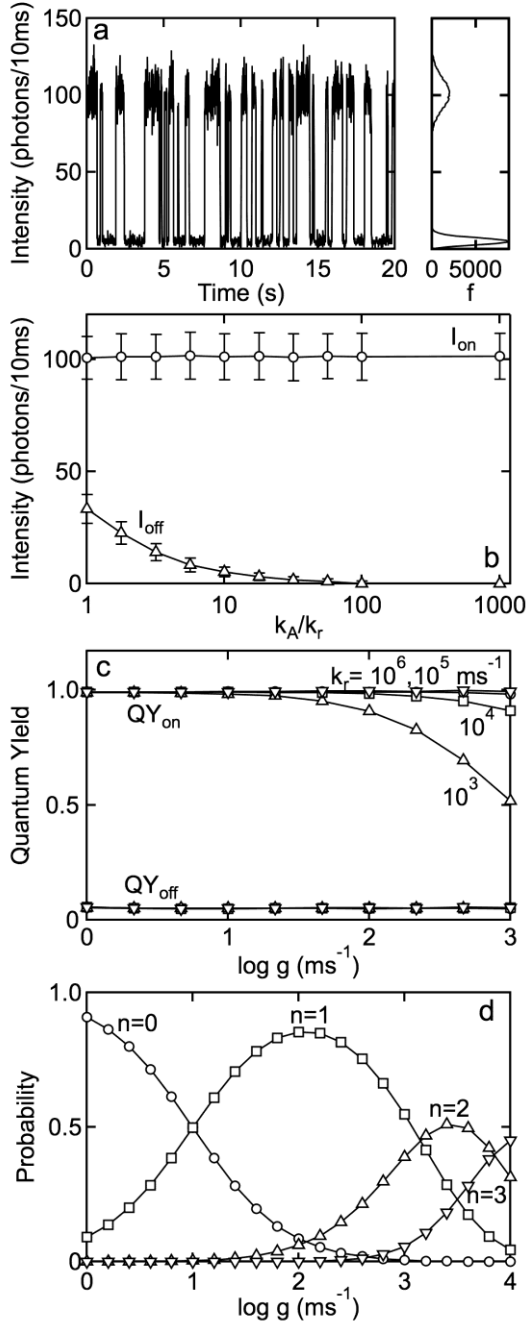
Figure 13. Influence of important rate constants on on and off intensities.

(a) Intensity-time curve (photons / 10 ms) and intensity distribution illustrating the gray state. The parameters are the same as for **Figure 12c** except that except that k_A is decreased from 10^7 ms^{-1} to 10^6 ms^{-1}. Other parameters are: $k_r = 10^5$ ms^{-1}, $g = 10$ ms^{-1}, $k_t = 10^0$ ms^{-1}, $k_d = 10^{-3}$ ms^{-1}, $k_{nrt} = 0$ ms^{-1}, and $s = 10$ with $r_{t,\text{eff}}/r_{d,\text{eff}} = 1$. (b) On and off intensities and their fluctuations versus k_A/k_r ($1 - 10^3$). Other parameters are the same as (a). (c) Quantum yield for on and off states versus generation rate g ($1 - 10^3$ ms^{-1}) at different radiative recombination rates ($k_r = 10^3 -$

10^6 ms^{-1}) with $k_A/k_r = 10$. Other parameters are: $s = 10$, $k_d = 10^{-3}$ ms^{-1}, $k_{nrt} = 0$ ms^{-1}, k_t chosen such that $r_{t,\text{eff}}/r_{d,\text{eff}} = 10^0$ and $P_{\text{on}} = 0.5$. (d) Probability of the steady state number of electron-hole pairs versus generation rate ($g = 1 - 10^3$ ms^{-1}), with other parameters the same as in (a).

The gray state is dependent primarily on k_A, k_r, and g. **Figure 13b** shows the magnitude of on and off intensities, as well as the amplitude of their fluctuations, plotted versus k_A/k_r ($k_r = 10^5$ ms^{-1}). For a bin time of 10 ms, the on intensity is ~ 100 photons/bin with fluctuations of ~ 10 photons/bin, independent of k_A/k_r. In the off state, the radiative and Auger recombination pathways operate in parallel, and hence we have:

$$QY_{\text{off}} = \frac{1}{1 + 2k_A / k_r} \quad \textbf{Equation 22}$$

Thus as $k_A \rightarrow k_r$, the QY$_{\text{off}}$ increases and reaches a value of 0.33 when $k_A = k_r$. Also note that when QY$_{\text{on}} = 1$ then QY$_{\text{off}} = I_{\text{off}}/I_{\text{on}}$.

When k_A/k_r is large, $I_{\text{off}}/I_{\text{on}} \rightarrow 0$, and the off state in an experiment would coincide with the background signal of the detector. In contrast, as $k_A \rightarrow k_r$, $I_{\text{off}}/I_{\text{on}}$ becomes significant so that the off state can be resolved above the background signal of the detector. In all cases, the on and off intensities and their fluctuations are not significantly influenced by the trapping and detrapping rate constants.

The influence of g and k_r on the on and off quantum yields for a typical grey state is shown in **Figure 13c**. The ratio k_A/k_r is maintained constant and the trapping rate constant is tuned so that the on-time fraction is always around 0.5 (**Figure 12**). As previously described, k_t, k_d and k_{nrt} only affect the on-time fraction. As the generation rate increases, QY$_{\text{off}}$ remains approximately constant at around 0.05. In contrast, QY$_{\text{on}}$ decreases above a characteristic value of g due to the presence of multiple e-h pairs (**Figure 13c**) and the increasing contribution of

Auger recombination (Klimov, Mikhailovsky et al. 2000, Kraus, Lagoudakis et al. 2005, Htoon, Malko et al. 2010).   When $g \rightarrow k_r$, the probability of creating more than one e-h pairs increases (**Figure 13d**), and hence the contribution from Auger recombination results in a decrease in QY_{on}.   For example, for $g = 10^3$ ms^{-1}, QY_{on} decreases from 0.98 when $k_r = 10^5$ ms^{-1}, to 0.5 when $k_r = 10^3$ ms^{-1}.

We next analyzed the number of e-h pairs in a QD under steady state conditions.   **Figure 13d** shows the probability of finding single or multiple e-h pairs for different generation rates. For low generation rates (≤ 1 ms^{-1}), radiative recombination is dominant and the probability of finding an e-h pair is low.   As the generation rate increases, the probability of finding multiple e-h pairs increases progressively and QY_{on} decreases (**Figure 13c**).   This effect was reported by Kraus et al. (Kraus, Lagoudakis et al. 2005) who showed that the PL intensity did not increase proportionally with increasing generation rate for CdSe/ZnS QDs.

2.2.3 Pulsed laser excitation

Experimentally, intensity-time curves are usually obtained under continuous excitation where $k_r > g$.   However, in some cases pulsed laser excitation is used to study blinking (Kraus, Lagoudakis et al. 2005, Peterson and Nesbitt 2008, Goushi, Yamada et al. 2009).   In these experiments, the laser pulse is typically on the order of picoseconds or less, much faster than other processes such as radiative recombination and Auger recombination, and the repetition time is typically on the order of microseconds.   In these experiments, multiple e-h pairs can be generated in each pulse before any relaxation process can occur.   The generation of multiple e-h pairs in a single pulse ($N_p \geq 2$) results in the instantaneous population of states where Auger recombination is significant.   As long as $k_A > k_r$, all additional electron-hole pairs in a pulse will

recombine very quickly, and the quantum yield in the on state is decreased; however, the blinking behavior is unchanged. When $k_A \approx k_r$, the additional *e-h* pairs can undergo radiative recombination and hence the on intensity will be higher than for continuous excitation with the same repetition time, even though the quantum yield for the pulsed experiment will be lower.

2.2.4 Power-law distributions of on and off times

With fixed values of k_t and k_d, the distributions of on and off times are exponential ($f = A\exp(-\tau/\tau_0)$). For example, **Figure 14b** shows an intensity-time curve and the distributions of on and off times for $k_t = 10^0$ ms^{-1} and $k_d = 10^{-3}$ ms^{-1}($k_{nrt} = 0$). The distributions are exponential with $\tau_{0,on} = 1.14 \pm 0.04$ s and $\tau_{0,off} = 1.17 \pm 0.08$ s ($P_{on} = 0.49 \pm 0.01$).

An exponential distribution of on and off times is expected for constant trapping and detrapping rates (Cook and Kimble 1985) as pointed out by Efros and Rosen (Efros and Rosen 1997), and has been observed experimentally for quantum jumps in atomic systems (Blatt and Zoller 1988). In practice, the distribution of on and off times obtained from analysis of intensity-time curves for QDs, usually exhibit power law behavior ($f = B\tau^{-\alpha}$) with exponents α typically between 1.0 and 2.0 (Kuno, Fromm et al. 2000, Kuno, Fromm et al. 2001, Hohng and Ha 2004, Crouch, Sauter et al. 2010).

Figure 14c shows the distribution of on and off times for a linear distribution of k_t and k_d (**Figure 14a** and **Table 3**), where k_t varies from 10^{-2} to 10^2 ms^{-1} and k_d varies from 10^{-5} to 10^{-1} ms^{-1}. For each trapping (detrapping) event the trapping (detrapping) rate constant is selected randomly over the given range, where all rate constants have equal probability. The distributions show power law behavior with $\alpha_{on} = 1.86 \pm 0.06$ and $\alpha_{off} = 1.86 \pm 0.03$ ($P_{on} = 0.52 \pm 0.05$).
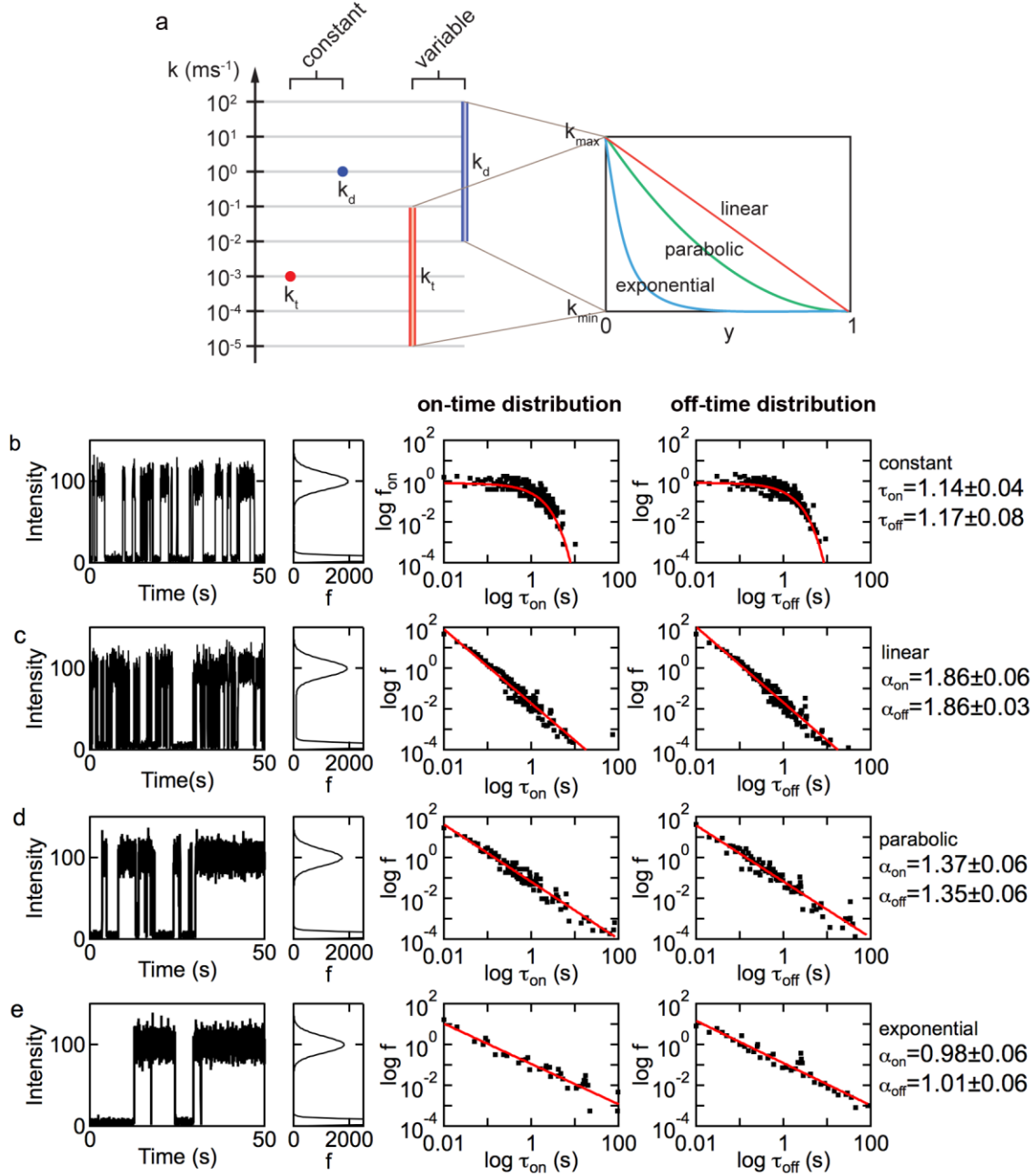
Figure 14. Simulated intensity-time curves, intensity distributions, and distributions of on and off times for QD excitation for constant and variable trapping and detrapping rate constants (k_t and k_d).

Here $k_{nrt} = 0$ ms^{-1}, $s = 10$, $k_r = 10^5$ ms^{-1}, $k_A = 10^7$ ms^{-1}, and $g = 10$ ms^{-1}. (a) The range and distribution of trapping and detrapping rate constants. (b) Constant trapping/detrapping rate constants: $k_t = 10^0$ ms^{-1}, $k_d = 10^{-3}$ ms^{-1}. (c) Linear distribution of trapping and detrapping rate constants: $k_t = 10^{-2} - 10^2$ ms^{-1}, $k_d = 10^{-5} - 10^{-1}$ ms^{-1}. (d) Parabolic distribution of trapping and

detrapping rate constants: $k_t = 10^{-2}$ - 10^2 ms^{-1}, $k_d = 10^{-5} - 10^{-1}$ ms^{-1}.   (e) Exponential distribution of trapping and detrapping rate constants: $k_t = 10^{-2} - 10^2$ ms^{-1}, $k_d = 10^{-5} - 10^{-1}$ ms^{-1}.

Function	Equation	a	b
Linear	$k = a(1-y) + b$	$k_{max} - k_{min}$	k_{min}
Parabola	$k = a(1-y)^2 + b$	$k_{max} - k_{min}$	k_{min}
Exponential	$k = a \cdot exp(-by)$	k_{max}	$\ln(k_{max}/k_{min})$

Table 3.   Variable trapping and detrapping rate constants.

Variations are defined by the range (k_{max} and k_{min}) and the function (linear, parabola, exponential), with respect to a stochastic variable y that varies from 0 to 1.0.   Here y represents either distance or energy.

The power-law exponent is dependent on the function that describes the distribution of trapping and detrapping rate constants.   For example, a parabolic distribution (**Figure 14d**) of k_t and k_d (over the same range), results in power-law distributions with $\alpha_{on} = 1.37 \pm 0.06$ and $\alpha_{off} = 1.35 \pm 0.06$ ($P_{on} = 0.42 \pm 0.14$).   An exponential distribution (**Figure 14e**) of k_t and k_d results in power-law distributions with $\alpha_{on} = 0.98 \pm 0.06$ and $\alpha_{off} = 1.02 \pm 0.06$ ($P_{on} = 0.52 \pm 0.15$).

To describe the influence of variable trapping and detrapping rate constants on the distribution of on and off times, it is convenient to refer to the effective trapping and detrapping rates ($r_{t,eff}$ and $r_{d,eff}$).   The range of trapping and detrapping rate constants gives rise to a range of $r_{t,eff}$ and $r_{d,eff}$.   Power-law behavior is only observed when there is a distribution of effective trapping and detrapping rates where $\tau_{t,eff}$ ($1/r_{t,eff}$) and $\tau_{d,eff}$ ($1/r_{d,eff}$) span a range from τ_{bin} to about $0.1\tau_{total}$.   For a typical bin time of 10 ms and a typical total time of 1000 s, this corresponds to a range of about 4 orders of magnitude.   The influence of the distribution of trapping and detrapping rate constants on the power law exponent is simply related to the distribution of

trapping events.   For example, a parabolic distribution has more events at longer times than a linear distribution which results in more probability density at longer times and hence a smaller slope.   Thus the range of power-law exponents observed experimentally can be obtained simply by tuning the function that described the range of trapping and detrapping rate constants.

2.2.5 Influence of trapping and detrapping times shorter than the binning time

A power law distribution of on and off times is obtained with a distribution of trapping and detrapping rates.   If the range of $\tau_{t,\mathrm{eff}}$ and $\tau_{d,\mathrm{eff}}$ extends to times shorter than τ_{bin} then we see the emergence of a third feature in the intensity distribution.   The trapping events at times faster than τ_{bin} give rise to an average on-intensity I_{av} due to switching within the binning time. Three-state blinking with an on state, an off state, and an average on state has been observed experimentally.   **Figure 15** shows intensity-time curves and the corresponding intensity distributions for simulations where we take a linear distribution of $\tau_{t,\mathrm{eff}}$ ($1/r_{t,\mathrm{eff}}$) and $\tau_{d,\mathrm{eff}}$ ($1/r_{d,\mathrm{eff}}$) but vary the range ($k_{\min}$ and $k_{\max}$).   All other parameters are the same as in **Figure 14c**.
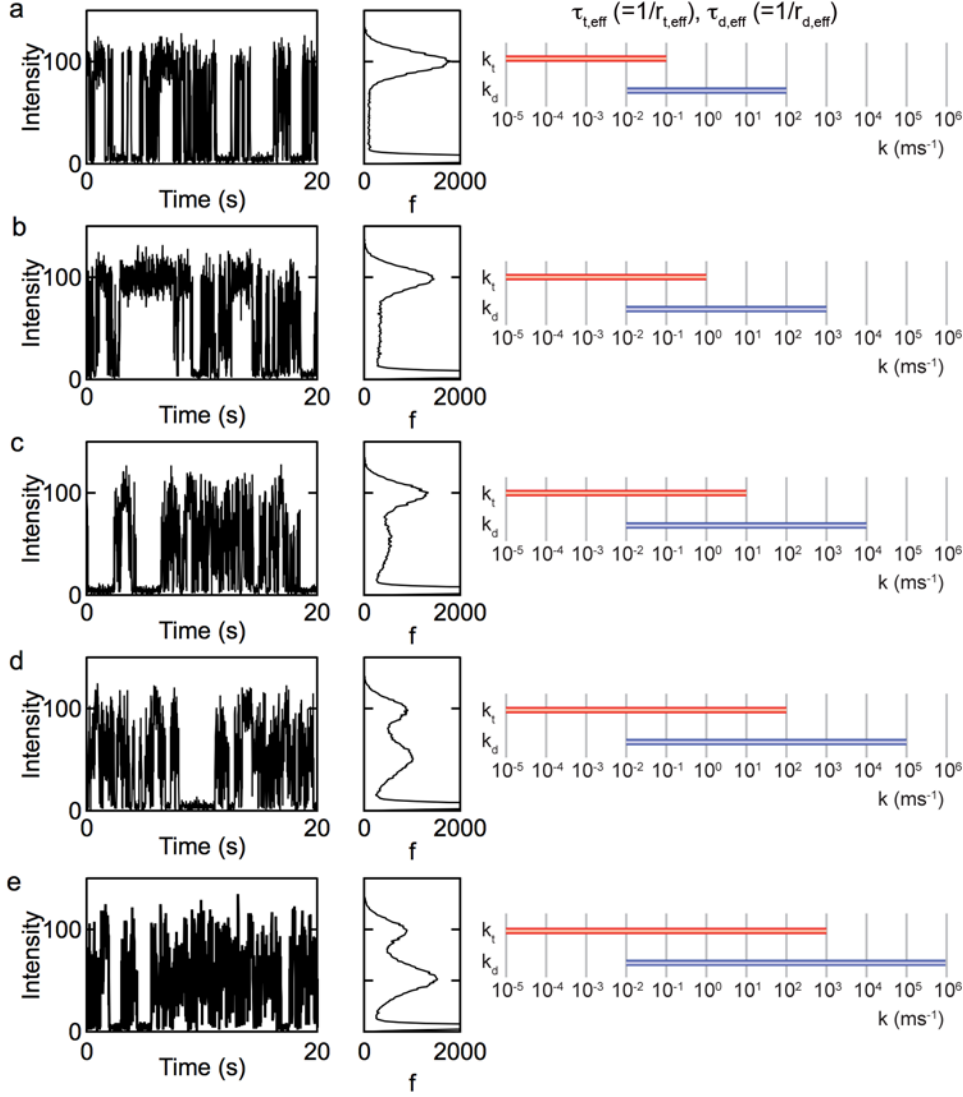
Figure 15. Simulated intensity-time curves, and intensity distributions as a function of trapping and detrapping times ($\tau_{t,\mathrm{eff}}$ and $\tau_{d,\mathrm{eff}}$).

Here $g = 10$ ms^{-1}, $k_r = 10^5$ ms^{-1}, $k_A = 10^7$ ms^{-1}, $s = 10$, $k_{nrt} = 0$ ms^{-1} for linear distributions of k_t and k_d. (a) $k_t = 10^{-5}$ to 10^{-1} ms^{-1}, $k_d = 10^{-2}$ to 10^2 ms^{-1}, (b) $k_t = 10^{-5}$ to 10^0 ms^{-1}, $k_d = 10^{-2}$ to 10^3 ms^{-1}, (c) $k_t = 10^{-5}$ to 10^1 ms^{-1}, $k_d = 10^{-2}$ to 10^4 ms^{-1}, (d) $k_t = 10^{-5}$ to 10^2 ms^{-1}, $k_d = 10^{-2}$ to 10^5 ms^{-1}, (e) $k_t = 10^{-5}$ to 10^3 ms^{-1}, $k_d = 10^{-2}$ to 10^6 ms^{-1}. In all cases the integration (bin) time was 10 ms.

Physically, a distribution in values of k_t and k_d is easily justified. For example, if trapping involves tunneling to trap states in the shell, then a distribution of distances from the QD core would be expected to give rise to a distribution in trapping and detrapping rates. Similarly, a

distribution in the energy of traps at the core/shell interface would be expected to give a distribution of trapping and detrapping rates.

2.3 Summary

Blinking ($k_A > k_r$)

        $k_A \gg k_r$ $I_{off}/I_{on} \approx 0$ no gray state

        $k_A \rightarrow k_r$ $I_{off}/I_{on} \rightarrow 0.33$ gray state

        $QY_{off} = 1 / (1 + 2k_A/k_r)$

        $QY_{on} \approx 1$ $(k_r > g)$ (decreases when $k_r \rightarrow k_A$ at high g)

Suppress blinking

        $\downarrow k_t$ and/or $\uparrow k_d$ $(k_t/k_d \rightarrow 1$ or $k_t > k_d)$

        $\uparrow k_{nrt}$ $(k_{nrt} > k_d)$

        $\uparrow k_r$ $(k_A > k_r)$

$$r_{t,eff} = \frac{sk_t g}{g + k_r} \qquad\qquad r_{d,eff} = \frac{(k_d + k_{nrt})(k_r + 2k_A)}{g + k_r + 2k_A}$$

$$P_{on} = \frac{r_{d,eff}}{r_{t,eff} + r_{d,eff}}$$

Distribution of on and off times

        Constant k_t, k_d $f = A\exp(-\tau/\tau_0)$

        Varying k_t, k_d $f = B\tau^\alpha$

        Power law exponent α dependent on distribution of k_t, k_d (k_{nrt})

Table 4. Summary of QD blinking behavior influenced by different processes.

Chapter 3 Endothelial Cells under Curvature and Shear Stress

To test the hypothesis that curvature and shear stress regulate endothelial cell morphology we developed the rod assay to mimic the cylindrical geometry of a blood vessel (**Figure 16**). While the rod assay is "inside out" in that the luminal sides of the cells are in contact with basement membrane on the rod, and the abluminal side is in contact with media, it is a convenient method to study the role of curvature on cell morphology over a wide range of diameters, from small capillaries to larger vessels.   Using this assay we show quantitatively that brain microvascular endothelial cells, in contrast to endothelial cells in other organs, do not elongate in response to curvature and shear stress.
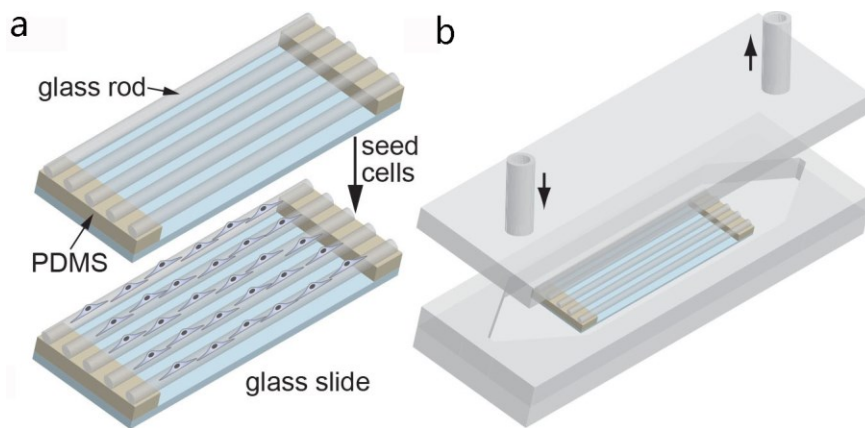
Figure 16.   Rod assay for studying the influence of curvature and shear stress on endothelial cells.

(a) In the rod assay, cells are seeded onto glass rods with different diameters and cell morphology determined from quantitative analysis of confocal microscope images.   (b) Schematic illustration of the microfluidic device incorporating an array of glass rods seeded with confluent monolayer of endothelial cells.

3.1 Materials and Methods

3.1.1 Rod assay

Glass rods 0.125 inches in diameter (Fisher Scientific, 11-380A) were pulled to a diameter in the range of 10 – 750 μm in a flame. The rods were cut into 2 cm lengths, selected for a particular diameter and uniformity under an optical microscope, and then mounted across two polydimethylsiloxane (PDMS) supports (Dow Corning, Sylgard 184) on a 22 mm x 22 mm glass slide (Fischer Scientific, 12542B). The rods were then immobilized with an additional drop of PDMS on top of the supports and cured at 80 ˚C for about 15 minutes. Prior to seeding cells, the rod assemblies were oxygen plasma cleaned for 30 seconds, and incubated in 150 μg ml^{-1} type I collagen (BD, 354236) solution in 0.02 M acetic acid (Fisher Scientific, A38-500) at room temperature for 1 to 2 hours, and then washed 3 times in PBS buffer (Corning Cellgro, 21-031-CV), followed by a final wash in cell culture medium.

3.1.2 Seeding cells

Human brain microvascular endothelial cells (HBMECs) were isolated from an adult brain and immortalized by transfection with SV40 (Nizet, Kim et al. 1997, Stins, Prasadarao et al. 1997, Eigenmann, Xue et al. 2013). HBMEC cell culture medium was prepared by dissolving HEPES-modified M199 powder (Sigma Aldrich, M2520) in 1 liter distilled water and adding 10 vol% FBS (Life Technologies, 16140071), 1 vol% penicillin-streptomycin (Life Technologies, 15140122), and 2.2 g l^{-1} sodium bicarbonate (Sigma Aldrich, S5761). Human umbilical vein endothelial cells (HUVECs, Lonza, CC-2517A) were suspended in the recommended cell culture medium (basal media with growth factors, Lonza, CC-3162). Human dermal microvascular endothelial cells (HMVECs, Life Technologies, C-011-5C) were cultured in medium prepared by dissolving 10 vol% FBS (Life Technologies, 16140071), 1 μg ml^{-1} hydrocortisone (Sigma

Aldrich, H0888), 2 U ml^{-1} heparin (porcine intestinal mucosa, sodium salt, Sigma Aldrich, H3149), 25 μg ml^{-1} endothelial cell growth supplement (Biomedical Technologies, BT-203), 0.2 mM L-ascorbic acid 2-phosphate (Sigma Aldrich, A8960), 1 vol% glutamine-penicillin-streptomycin (Life Technologies, 10378-016) in MCDB 131 (Caisson Labs, MBL02). All endothelial cells were routinely passaged at a 1:4 ratio, and were discarded after passage 5.

Approximately 10^6 cells in 2 ml of medium were introduced into each dish containing a set of collagen-coated rods. The cell culture medium was changed every day by adding 2 - 3 ml of fresh medium into the petri dish, mixing it well, removing the same amount, and repeating at least 3 times. The cells generally began to spread on the rods after one day and if the coverage was about 60 %, and reached confluence after 3 – 4 days. For control experiments in 2D, glass bottom petri dishes (BD, FD35PDL-100) were plasma treated for 30 seconds, coated with 150 μg ml^{-1} type I collagen (BD, 354236) solution in 0.02 M acetic acid for 1 – 2 hours, and washed 3 times with PBS and once in cell culture medium prior to seeding with cells.

3.1.3 Shear stress

To study the effects of shear stress and curvature, a set of 200 μm rods was located parallel to the flow direction in a custom microfluidic device 40 mm long, 10 mm wide, and 2 mm high. The rods were typically 100 μm from the bottom of the channel. The device was placed in an incubator maintained at 37 ˚C and 5% CO_2. Experiments were performed at a constant flow rate of 640 ml min^{-1} using a peristaltic pump (Cole Parmer, WU-07523-80). The wall shear stress for a Newtonian fluid is given by $\tau = 6\mu Q/(wh^2)$, where μ is the viscosity (0.001 Pa s), Q is the flow rate, w is the channel width, and h is the channel height. From COMSOL simulations

(**Figure 17**) we determined that the shear stress on the upper quadrant of the rods was 50 dyne cm^{-2}, decreasing to about 25 dyne cm^{-2} at the sides.   Quantitative analysis of morphology was performed for cells on the upper quadrant.   After seeding cells on the rods and allowing them to reach confluence, the flow rate was set to about 40 ml min^{-1} for 1 hour, and then gradually increased to 640 ml min^{-1} over 6 hours, and then maintained at this value for 24 hours prior to removing the rods for analysis.
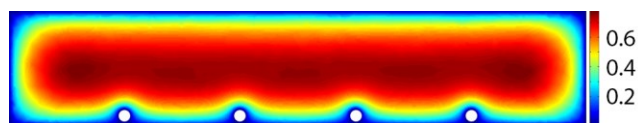
Figure 17.   Cross-section velocity profile in a microfluidic channel.

Cross-section velocity profile (m/s) around 200 μm diameter glass rods located 100 μm above the bottom of a microfluidic channel.

3.1.4 Imaging

Cells on collagen-coated rods were fixed and stained for ZO-1 (BD, 610967) or VE-cadherin (Life Technologies, 61-7300) and DAPI (Sigma Aldrich, D9542-1MG).   Cell monolayers on rods were imaged using a confocal microscope (Zeiss LSM 510 META).   Before imaging, the glass rods were removed from the assembly and placed on a 170 μm thick glass bottomed petri dish (World Precision Instruments, FD5040-100), and incubated in 2, 2′ – thioldiethanol (Sigma Aldrich, 166782).   All images were obtained using a 40X oil-immersion objective (40X 1.3 NA Plan Neofluar (oil)) in immersion oil (Zeiss, 444963-0000-000).   Matching the refractive index of the rods is important to minimize distortion of the images.   Z-stack images (512 x 512 pixel) were taken at 0.3 – 1.2 μm steps depending on the rod diameter.

3.1.5 Image analysis

For quantitative analysis of cell morphology the cylindrical immunofluorescence images of the cell monolayers were converted to a 2D plane using UNWRAP a custom application developed in our lab (**Figure 18**).   Morphological analysis was performed on the unwrapped 2D images using ImageJ (National Institute of Health, Bethesda, MD).   After identification of the cell-cell boundaries, we determined projected cell area (μm^2), perimeter (μm), inverse aspect ratio (IAR) (length of short axis / length of long axis), and the orientation angle (θ), i.e. the angle between the cell long axis and the rod axis (0 to 90 degrees).   The number of cells around the perimeter of the cylinder was determined by selecting a line perpendicular to the rod direction and counting the number of cells on the line.   The line was then moved along the image in the direction of the rod axis until there were no previously counted cells along the line.   For a given unwrapped image corresponding to a rod segment, we can usually extract about 3 – 4 measurements from each image.   For HBMECs we made 14 – 62 measurements for each rod diameter (total = 303) and for HUVECs we made 18 – 117 measurements (total = 531).

The distribution of actin stress fibers was analyzed by performing 2D FFTs on the images. FFTs were performed using the FFT2 routine in MATLAB.   The resulting intensity distributions in the frequency domain were converted to radial intensity distributions at 10˚ increments.   For images on larger rods and 2D images were cropped to be 141 x 141 μm the resolution fixed at 0.44 μm per pixel.   For images on smaller rods, images were cropped to be 93 x 93 μm with the resolution fixed at 0.44 μm per pixel.

Welch two sample t-tests were performed in MATLAB.   Significant levels were determined between samples examined and were set at * $P < 0.05$, ** $P < 0.01$, and *** $P < 0.001$.

(a) construct cylinder (or partial cylinder) from z-stack images

(b) select locations to construct cross sections

(c) define circle at focal plane of interest for unwrapping

(d) unwrapped image
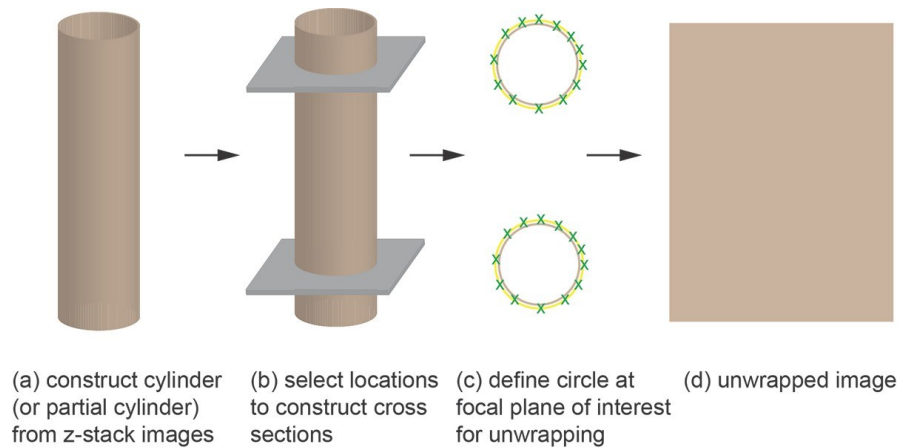
Figure 18.   Workflow of UNWRAP.

The immunofluorescence images are transposed onto a 2D plane using custom software – UNWRAP.

3.2 Results and Discussion

Human brain microvascular endothelial cells (HBMECs) were seeded onto glass rods with diameters from 10 – 500 µm, spanning the range from brain capillaries to larger vessels, and allowed to reach confluence.   For comparison, experiments were also performed with HUVECs, widely used in cell culture studies of endothelial cells.   Typical confocal microscope images of cells seeded onto rods with different diameters are shown in **Figure 19a-f**.   To visualize the cell boundaries we stained for the tight junction protein ZO-1 in HBMECs and VE-cadherin in HUVECs.   The junctional markers reveal the morphology of the cells on the surface of the rods. At the smallest rod diameters, the HBMECs wrap around to form junctions with themselves (**Figure 19c** and **Figure 19i**), whereas the HUVEC cells do not (**Figure 19f** and **Figure 19l**).
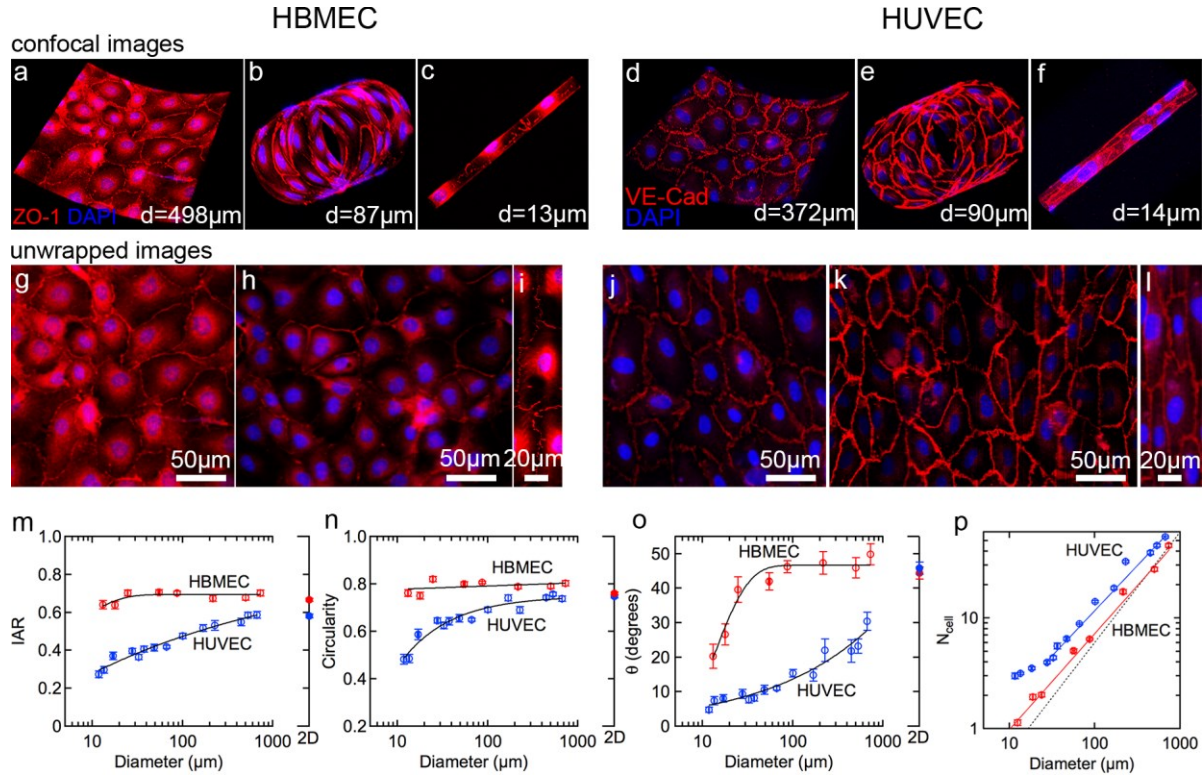
Figure 19. Influence of curvature on morphology of HBMEC and HUVEC confluent monolayers.

(a-f) Confocal microscope images of confluent monolayers of HBMECs and HUVECs on rods with different diameters. (a-c) **HBMECs:** (a) d = 498 µm, (b) d = 87 µm, (c) d = 13 µm. ZO-1 (red), DAPI (blue). (d-f) **HUVECs:** (d) d = 372 µm, (e) d = 90 µm, (f) d = 13.7 µm. VE-Cadherin (red), DAPI (blue). Scaling in xy direction 0.44 µm/pixel, scaling in z direction 0.8 µm/pixel.

(g-l) Unwrapped confocal microscope images of confluent monolayers of HBMECs and HUVECs on rods with different diameters.

(m-o) Cell morphology for confluent monolayers of HBMECs and HUVECs on rods with different diameter. Data for 2D confluent monolayers are shown for comparison. Inverse aspect ratio is the length of the short axis divided by the length of the long axis, circularity, $C = 4\pi A/P^2$, and the angular orientation is with respect to the rod axis. The total number of cells analyzed was 666 (HBMEC) and 1018 (HUVEC). Error bars represent SE.

(p) Average number of cells around the rod perimeter for HBMECs and HUVECs. The solid lines show fits to a power law where $N_{cell} \propto d^{\alpha}$. For HBMECs $\alpha = 0.86$ and the intercept where $N_{cell} = 1$ is at d = 9.8 µm. For HUVECs, $\alpha = 0.80$ and the intercept where $N_{cell} = 1$ is at d = 4.4 µm. The dotted line shows $\alpha = 1.0$. Error bars represent SE.

The immunofluorescence images are transposed onto a 2D plane (**Figure 19g-l**) using UNWRAP.   Image analysis software (e.g. ImageJ) is then used for quantitative analysis of cell morphology on the "unwrapped" images.   Using this   approach we can quantitatively determine parameters associated with cell morphology such as the projected cell area (A), perimeter (P), circularity ($C = 4\pi A/P^2$), inverse aspect ratio (IAR, length of short axis divided by length of long axis), and the orientation angle of the cell long axis with respect to the rod axis (θ). We also used these unwrapped images for quantitative analysis of actin filament orientation using Fourier transformation.

3.2.1 Elongation and alignment

The dependence of morphological parameters on rod diameter for immortalized HBMECs and HUVECs is summarized in **Figure 19m-p**.   Data for 2D monolayers are provided for comparison (**Figure 20**) and additional data on cell area and perimeter are provided in **Figure 21**. For HBMECs, the inverse aspect ratio (IAR), a measure of cell elongation, is only weakly dependent on curvature (**Figure 19m**).   For rod diameters larger than 25 μm, the IAR is about 0.7, independent of diameter, whereas for rod diameters less than 25 μm, the IAR decreases slightly to about 0.65 at a diameter of about 10 μm.   In contrast, the IAR for HUEVCs is strongly dependent on curvature, decreasing from about 0.6 at the largest diameter (d > 400 μm) to about 0.2 at the smallest rod diameter (d ≈ 10 μm) (**Figure 19m**).   Similar trends are observed for the cell circularity, a parameter commonly used in measuring cell morphology (**Figure 19n**).   The small changes in IAR and circularity of HBMECs indicate that they are not sensitive to curvature and elongate only slightly as the rod diameter decreases below 25 μm.
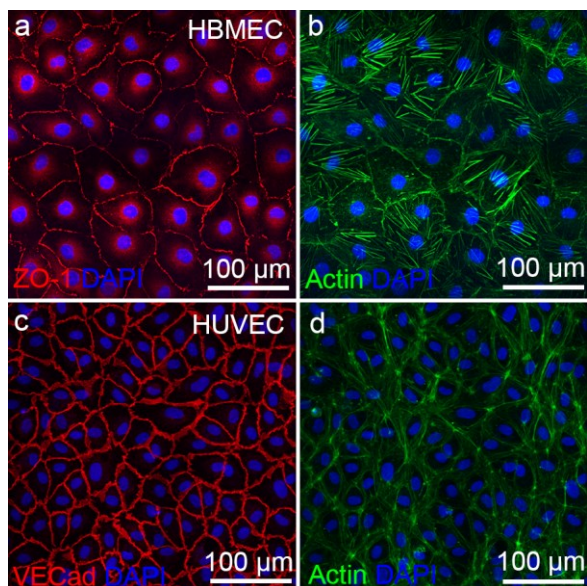
Figure 20. Fluorescence images of confluent monolayers of HBMECs and HUVECs in 2D.

HBMECs: (a) ZO-1 (red), DAPI (blue); (b) actin (green), DAPI (blue). HUVECs: (c) VE-cadherin (red), DAPI (blue); (d) actin (green), DAPI (blue).
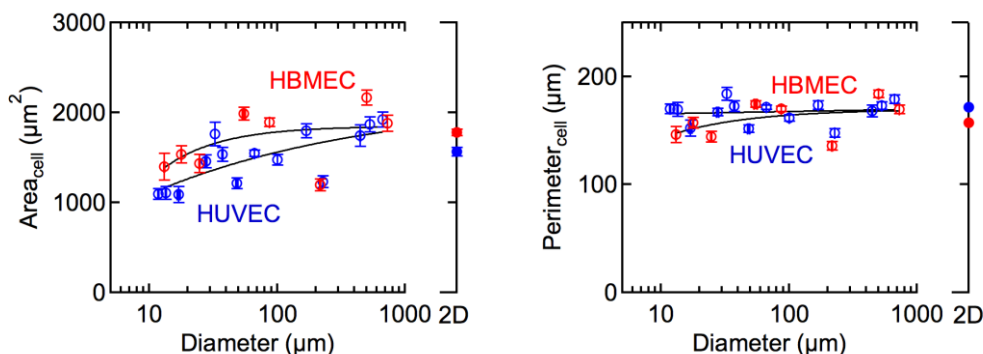
Figure 21. Cell area and perimeter for HBMECs and HUVECs on rods with different diameter and in 2D.

The average orientation angle of HBMECs is a measure of the axial alignment of cells (**Figure 19o**). On large diameter rods and in 2D monolayers, the average orientation angle is 45˚, characteristic of a random distribution between $0 - 90$˚ across all cells. The orientation remains random for rod diameters down to about 25 μm, further supporting the conclusion that the HBMECs are relatively insensitive to curvature. For rod diameters less than 25 μm, the

average orientation angle decreases very rapidly to around 15˚ as the diameter approaches 10 μm.

In contrast, the average orientation angle of HUVECs decreases very quickly, reaching a value of less than 15˚ at a rod diameter of about 200 μm, and approaching 0˚ for the smallest diameter (11 μm). Even on the largest diameter rods, the curvature is sufficient to cause significant cell alignment. In summary, HUVECs are extremely sensitive to curvature, and begin to elongate and align even at the largest rod diameters. At the smallest diameters, the IAR decreases to about 0.2 corresponding to an elongation of five times, and the average orientation angle approaches zero corresponding to almost complete alignment.

The effect of curvature on endothelial cell morphology can be compared to the effect of shear stress. Analysis of endothelial cells in aortic vessels of dogs and rabbits reveals an IAR ≈ 0.2 (C ≈ 0.3) and an average orientation angle of 5 − 15˚ (Silkworth, Stehbens et al. 1975, Nerem, Levesque et al. 1981, Levesque and Nerem 1985). These values for IAR and orientation angle are similar to those reported here for HUVECs on rod diameters of about 10 μm suggesting that curvature has a similar effect to shear stress in vivo. In 2D cell culture, bovine aortic endothelial cells and HUVECs are characterized by IAR ≈ 0.7 (C ≈ 0.8) and θ ≈ 45˚ (Levesque and Nerem 1985, Malek and Izumo 1996). However, under a shear stress of $20 − 85$ dynes cm^{-2} for 24 h, the IAR decreases to about 0.25 (C ≈ 0.4) and θ to about 15˚ (Malek and Izumo 1996), further suggesting that curvature and physiological shear stress have a similar effect on cell morphology.

3.2.2 Scaling

In brain capillaries, HBMECs wrap around the capillary perimeter to form tight junctions with themselves as well as their neighbors. To investigate how endothelial cells arrange themselves as the rod diameter decreases, we analyzed the number of cells around the perimeter of the rods (**Figure 19p**). For HBMECs, the number of cells around the perimeter (N_{cell}) of the rod decreases with decreasing radius, following a power law ($N_{cell} \propto d^{\alpha}$) with an exponent $\alpha = 0.86$, down to the smallest diameter where cells wrap around the rod to form junctions with themselves and their neighbors as in brain capillaries. The x-axis intercept at $N_{cell} = 1$ (i.e. a single cell wrapping around to form a junction with itself) corresponds to a rod diameter of 9.8 μm, very close to typical human brain capillary dimensions. For a fixed IAR and projected cell area, the number of cells around the perimeter of a rod is expected to decrease linearly with diameter with an exponent $\alpha = 1.0$. The exponent of 0.86 is consistent with the small elongation.

The number of HUVEC cells around the perimeter also follows a power law down to about 30 μm in diameter with an exponent of 0.80. The decrease in IAR (**Figure 19m**) and projected cell area both contribute to the smaller exponent compared to HBMECs. For rod diameters less than about 30 μm, the number of cells around the perimeter does not decrease below 3, indicating that there is a larger energy barrier for HUVECs to spread in regions of very high curvature compared to HBMECs (**Figure 30**). Furthermore, the x-axis intercept at $N_{cell} = 1$ corresponds to a rod diameter of 4.4 μm, below the typical human capillary diameter of around 8 μm, suggesting that HUVECS would not be able to wrap around and form junctions with themselves in capillaries, even without the deviation from power law behavior.

3.2.3 Finite size effects in orientation angle

The orientation angle of a cell is defined as the angle between the cell long axis (ℓ) and the

rod axis (**Figure 22**). On large rods where the perimeter is much larger than the long axis of the

cell ($\pi d \gg \ell$), the cell can adopt any orientation angle between 0° and 90°. For a uniform

distribution of orientation angles, the average value is 45°. If there is an energy barrier (**Figure**

8) to wrapping around the perimeter of the vessel then the cells will be preferentially aligned

along the vessel axis and the average orientation angle will be less than 45°. However, when

the rod perimeter is less than the long axis of the cell ($\pi d \leq \ell$), then large angles are prohibited

and the maximum allowed orientation angle is less than 90°, and hence the average angle is also

less than 45°.
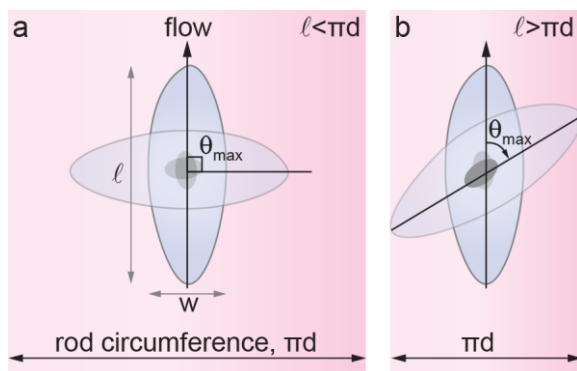
Figure 22. Schematic illustration showing how the finite size of a rod can limit the distribution of orientation angles of an endothelial cell.

On large rods where the perimeter is much larger than the long axis of the cell ($\pi d \gg \ell$), the cell can adopt any orientation angle between 0° and 90°. When the rod perimeter is less than the long axis of the cell ($\pi d \leq \ell$), large angles are prohibited.

The influence of curvature and finite size effects on the average orientation angle can be seen

in scatter plots of cell length and orientation angle for individual cells on a given rod diameter

(**Figure 23**). HBMEC cells span the full range of allowed angles on large diameter (499 μm) glass rods. For the range of cell lengths, approximately 40 – 80 μm, all orientation angles are allowed and the average angle is about 45˚. On small diameter (18 μm) rods, the HBMECs span the full range of allowed angles, however, for the longer cells higher orientation angles are prohibited. HUVEC cells on large diameter (530 μm) rods exhibit the full range of orientation angles, although the frequency at smaller angles is significantly higher due to curvature driven alignment. On small diameter rods (13 μm) the HUVECs exhibit orientation angles considerably lower than the allowed range, illustrating the effect of curvature on cell alignment. In summary, the decrease in average orientation angle for HBMECs at small diameters is due to a finite size effect and not due to the influence of curvature. In contrast, the decrease in angle for HUVECs is due to curvature.

Figure 23. Cell length and orientation angle for HBMECs and HUVECs on small and large diameter rods.

(a) HBMECs on 18 ± 0 μm (SE) glass rods (N = 66), (b) HBMECs on 499 ± 0 μm (SE) rods (N = 76), (c) HUVECs on 13 ± 0 μm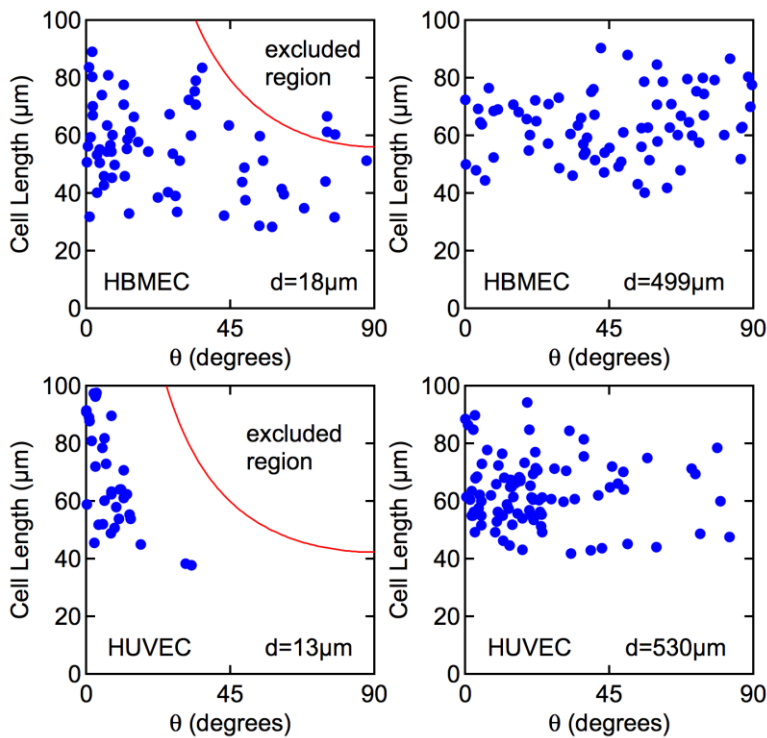 (SE) rods (N = 39), and (d) HUVECs on 530 ± 1 μm (SE) rods (N = 92).   The solid lines represent $\ell\sin\theta = \pi d$ where d is the average rod diameter.   A cell of length ℓ can adopt any orientation angle θ on a rod of diameter d as long as $\ell\sin\theta \leq \pi d$. When the cell length is larger than πd then all orientation angles are allowed, however, when $\ell \leq \pi d$ then some angles are prohibited.   This finite size effect leads to a change in the distribution of orientation angles and a decrease in the average orientation angle.   SE is the standard error.

3.2.4 Shear stress

To assess the influence of curvature and shear stress on cell morphology, we subjected approximately 250 μm diameter rods with confluent monolayers of HBMECs and HUVECs to a shear stress of about 50 dyne cm^{-2} for 24 hours (**Figure 24**).   Analysis of cell morphology revealed no significant change in IAR, circularity, or alignment for HBMECs.   In contrast, HUVEC cells showed a significant increase in elongation and alignment under shear stress compared to static conditions.   However, these changes were smaller than induced by curvature, further highlighting the important role for curvature in regulating cell morphology.   For example, the IAR of HUVECs on 228 μm rods decreased from 0.53 under static conditions to 0.36 under shear stress (**Figure 24e**).   In contrast, the IAR decreased from 0.58 in 2D confluent monolayers to 0.27 on 12 μm diameter rods under static conditions (**Figure 24m**).

The distribution of actin stress fibers in the cells also shows significant differences between HBMECs and HUVECs.   In HBMECs, the stress fibers are oriented in all directions but with noticeably more fibers aligned perpendicular to the rod axis.   In contrast, the stress fibers in HUVECs are predominantly aligned along the rod axis.   In 2D experiments with bovine aortic endothelial cells and HUVECs, shear stress results in a reversible transition from a cobblestone morphology to a spindle morphology with the long axis aligned in the direction of flow.   At the same time there is a reorganization in the actin cytoskeleton resulting in the formation of bundles

of stress fibers aligned in the direction of flow (Franke, Grafe et al. 1984, Malek and Izumo 1996).   The different alignment of stress fibers suggests that curvature influences cytoskeleton organization.   This may be similar to the way that mechano-transduction of shear stress associated with blood flow plays a role in the regulation of physical, biochemical, and gene expression responses in arterial circulation (Davies 1995, Chien 2007, Hahn and Schwartz 2009).
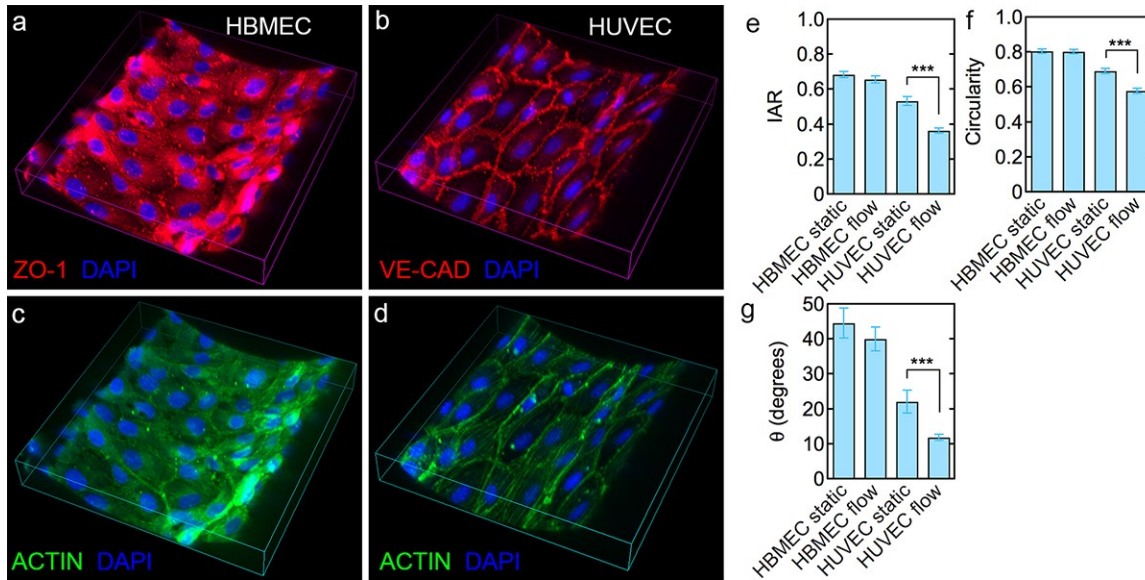
Figure 24.   Influence of shear stress and curvature on cell morphology.

Cells were seeded on rods with average diameter of 217 ± 0 µm (HBMEC) and 228 ± 1 µm (HUVEC) and subjected to a shear stress of 50 dyne cm^{-2} for 24 hours.   (a, c) HBMEC, (b, d) HUVEC, (e) IAR, (f) circularity, and (g) average orientation angle.   HBMEC static (N = 72), HBMEC shear stress (N = 45), HUVEC static (N = 46), HUVEC shear stress (N = 92).   *** P < 0.001.   For HUVEC: P = 1.2 x 10^{-7} (IAR), P = 2.4 x 10^{-7} (C), P = 3.9 x 10^{-3} (θ). Error bars represent SE.

3.2.5 Alignment of actin filaments

The differences in cell morphology between HBMECs and HUVECs are associated with differences in the actin cytoskeleton (**Figure 25**).   In HBMECs, actin stress fibers in the cell appear preferentially oriented perpendicular to the rod axis around the circumference (**Figure**

25b and **Figure 25d**). This is particularly striking for the smallest rod diameters (**Figure 25f** and **Figure 25h**). In contrast, the stress fibers in HUVECs appear preferentially oriented in the axial direction (**Figure 25k** and **Figure 25m**), and this is particularly evident at small rod diameters (**Figure 25o** and **Figure 25q**).

Figure 25. Confocal microscope images of HBMECs and HUVECs on large and small diameter glass rods.

HBMECs on a 170 μm diameter rod: (a) ZO-1 (red), DAPI (blue); (b) actin (green), DAPI (blue); (c, d) corresponding unwrapped images. HBMECs on an 11 μm diameter rod: (e) ZO-1 (red), DAPI (blue); (f) actin (green), DAPI (blue); (g, h) corresponding unwrapped images; (i) cross-section ZO-1 (red), actin (green), DAPI (blue).

HUVECs on a 228 μm diameter rod: (j) VE-cadherin (red), DAPI (blue); (k) actin (green), DAPI (blue); (l, m) corresponding unwrapped images. HUVE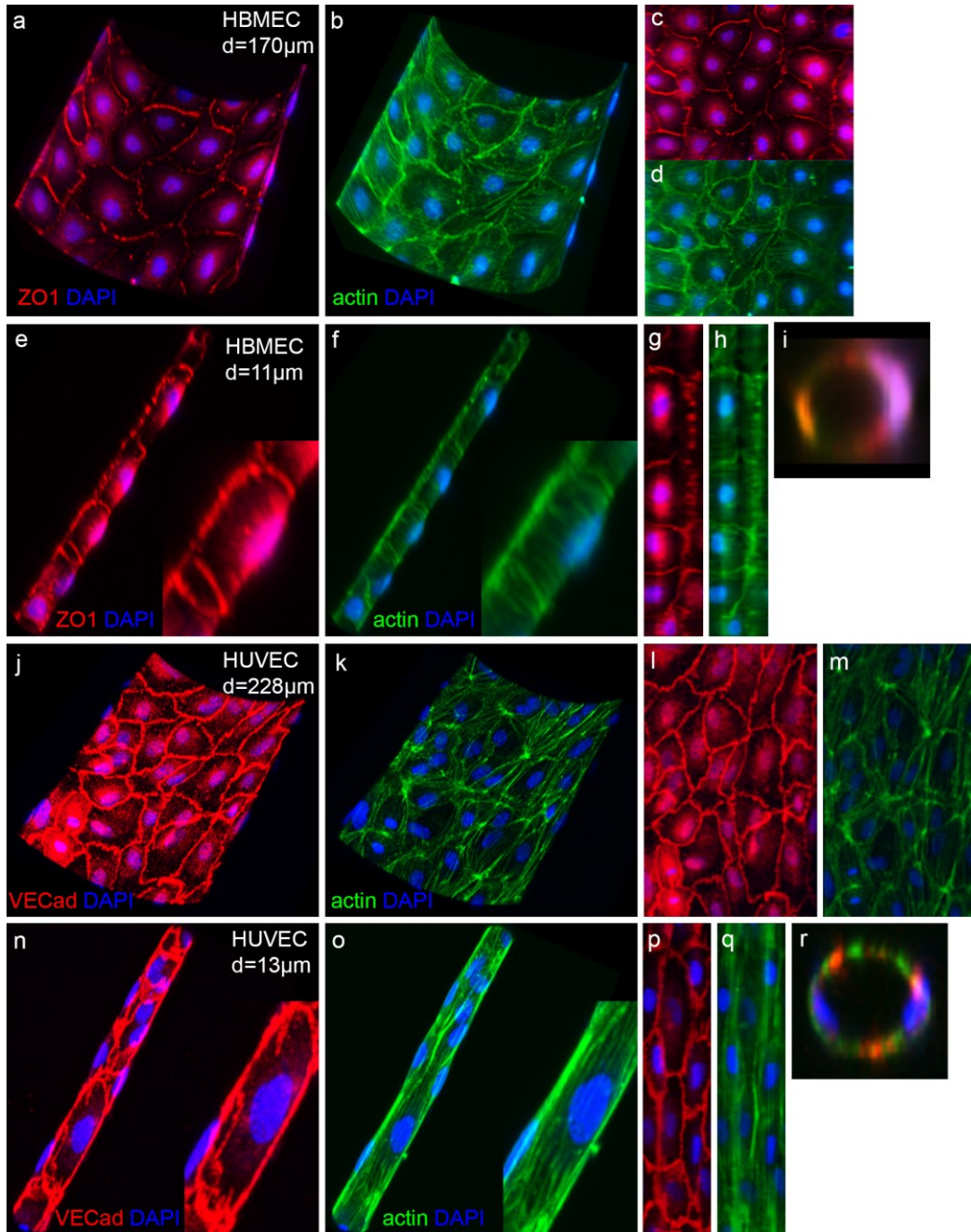C on a 13 μm diameter rod: (n) VE-cadherin (red), DAPI (blue); (o) actin (green), DAPI (blue); (p, q) corresponding unwrapped images; (r) cross-section VE-cadherin (red), actin (green), DAPI (blue).

To quantitatively analyze actin filament alignment, we determined the radial intensity distribution from fluorescence images using fast-Fourier transforms. We compared HBMEC and HUVEC cells in 2D confluent monolayers and on rods under static and flow conditions. Fluorescence images of cells in 2D and on larger rods (d ≈ 200 μm) were cropped to be 141 x 141 μm with a resolution of 0.44 μm per pixel. Images of cells on smaller rods (d ≈ 10 μm) were cropped to be 41 x 41 μm with a resolution of 0.44 μm per pixel. The input images were cropped to be square to ensure equal contributions from vertical and horizontal axes.

We obtained the largest square image for each experimental condition, resulting in 5 cropped images for HUVEC and HBMEC cells in 2D, and 4 cropped images for HUVEC and HBMEC cells on large diameter rods (d ≈ 200 μm), and 5 cropped images for HUVEC and HBMEC cells on small diameter rods (d ≈ 10 μm).

Control experiments. To study how image area influences the radial distribution in the frequency domain, we cropped the image of HUVEC cells in 2D into 4 small squares, and compared the radial distribution in the frequency domain, and found that the relative change is less than 20%, smaller than the relative difference between cells in different conditions (e.g. HUVEC cells on large diameter rods under static conditions compared to small diameter rods under static condition). To study how the resolution influences the radial distribution in the

frequency domain, we compared the images of HUVEC cells in 2D at resolutions of 0.36 and 0.44 μm per pixel. The relative change in radial distribution in the frequency domain was less than 15%.

The square images, $f(x, y)$ ($0 \leq x, y \leq N-1$, N is the number of pixels for the image square) were transformed into the frequency domain using fft2 in MATLAB. The FFT image was produced by shifting $F(0, 0)$ to the middle using fftshift, and calculating the magnitude of $F(u, v)$ - $|F(u, v)|$ using the abs routine in MATLAB.

The actin stress fibers in the fluorescence images can be considered as a superimposition of 2D intensity waves, whereas each pixel in the frequency domain ($|F(u, v)|$) can be considered as a single wave of intensities in frequency domain. The intensity for each pixel in the frequency domain, $|F(u, v)|$, represents the strength of each single wave. To characterize the directionality of the actin stress fibers in the fluorescence image, we divided the FFT image into 18 bins, each with an angular range of 10˚, and the intensities in each bin were added together, and divided by the total intensities of all bins (the center pixel or pixels excluded). The intensity fraction of all bins was plotted as a bar graph. If the actin stress fibers were uniformly distributed in the fluorescence image, each bin is expected to have an intensity fraction of about 5.6% ($\approx 100/18$) (see dotted line in bar graphs in **Figure 26**).

The actin fiber alignment is determined from the parallel and perpendicular indices. The parallel index represents the degree of alignment of actin fibers along the rod axis (vertical) and is defined by the sum of the intensities at 0 ± 10˚ (i.e. the sum of the intensities in the $0 - 10$˚ and $170 - 180$˚ bins). The perpendicular index represents the degree of alignment perpendicular to the rod axis (horizontal) and is defined by the sum of the intensities at 90 ± 10˚ (i.e. the sum of the intensities in the $80 - 90$˚ and $90 - 100$˚ bins).

For HBMEC and HUVEC cells in 2D the radial distributions show no preferential alignment – the parallel and perpendicular indices are about 11%, characteristic of a uniform distribution (100%/9). For HBMECs on rods, both the parallel and perpendicular indices increase with decreasing diameter, indicating both parallel and perpendicular alignment of the actin filaments. In contrast, for HUVECs on rods, the parallel index increases significantly with decreasing diameter, showing strong axial alignment. For HBMEC cells on large diameter rods ($d \approx 200$ µm), shear stress results a small decrease in the perpendicular index and a larger increase in the parallel index. Similar results are observed for HUVECs.
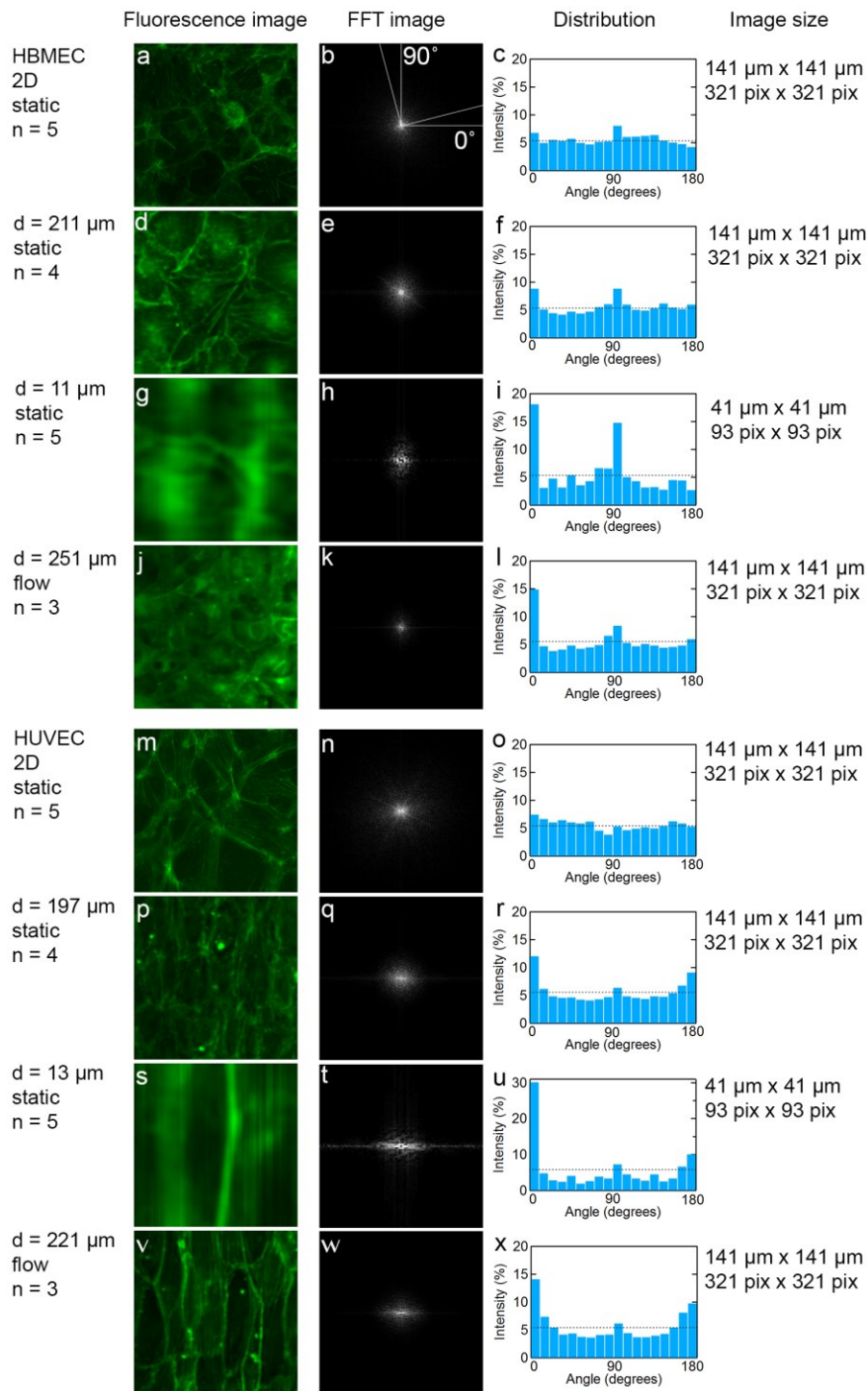
Figure 26. Quantitative analysis of actin fiber alignment.

Fluorescence images of confluent monolayers of HBMEC and HUVEC cells in 2D, and on large (d ≈ 200 µm) and small (d ≈ 10 µm) diameter rods under static conditions.   Also shown are fluorescence images of HBMECs and HUVECs on large diameter rods under shear stress (d ≈

200 µm).   All images were saved at a resolution of 0.44 µm per pixel.   The FFT images show
the distribution of intensity in reciprocal space, with the zero-frequency pixel in the center.   The
bar graphs show the radial intensity distributions.
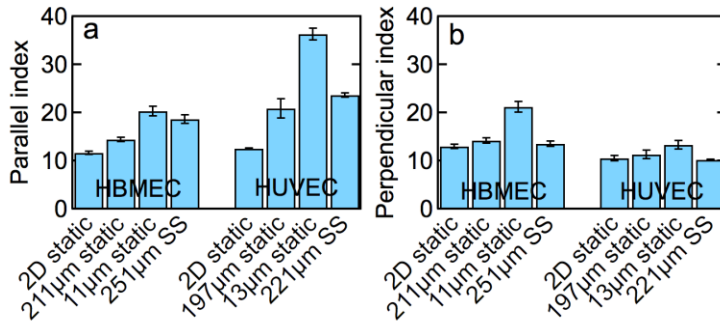
Figure 27.   Parallel and perpendicular indices for actin fiber distribution.

Data obtained from analysis of the radial intensity distributions for confluent monolayers of
HBMEC and HUVEC cells in 2D, on large and small diameter rods under static conditions, and
on large diameter rods under shear stress (SS).   The average index for no preferential
orientation is 11.1 (100%/9). HBMECs: (2D static) image number = 5; (211 µm static) d = 211 ±
14 µm (SE), image number = 4; (11 µm static) d = 11 ± 0 µm (SE), image number = 5; (251 µm
SS) 251 ± 2 µm (SE), image number = 3.   HUVECs: (2D static) image number = 5; (197 µm
static) d = 197 ± 14 µm (SE), µm (SE), image number = 3.

3.2.6 Non-brain vessels

Assuming that HBMECs and HUVECs are representative of endothelial cells in brain

microvessels and non-brain large vessels, respectively, then the cell morphology and distribution

of actin stress fibers suggest that endothelial cells in brain microvessels may be programmed to

respond to curvature differently than endothelial cells in larger vessels.   To compare the

behavior of endothelial cells in brain and non-brain microvessels, we studied the morphology of

human dermal microvascular endothelial cells (HMVECs) in 2D and on glass rods with

diameters around 20 and 200 µm (**Figure 28** and **Figure 29**).   These results show that

HMVECs behave similarly to HUVECs in all conditions, with morphological parameters (i.e.

IAR, circularity, and orientation angle) significantly different from HBMECs in response to

curvature (P < 0.001).   This suggests it is the organ (brain or non-brain) rather than the vessel

size that dictates the endothelial cell phenotype.
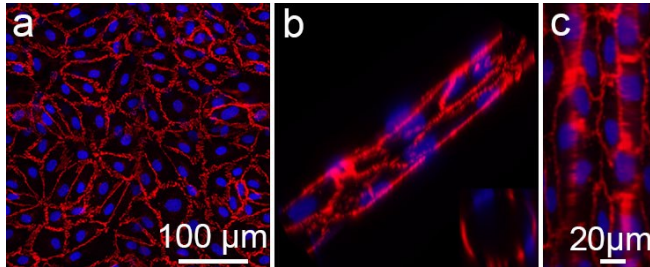
Figure 28.   Fluorescence images of confluent monolayers of human dermal microvascular endothelial cells (HMVECs) in 2D and on a 24 μm diameter rod.

(a) HMVECs in 2D.   (b) HMVECs on a 24 μm diameter rod.   (c) Corresponding unwrapped image for (b).   VE-cadherin (red), DAPI (blue).
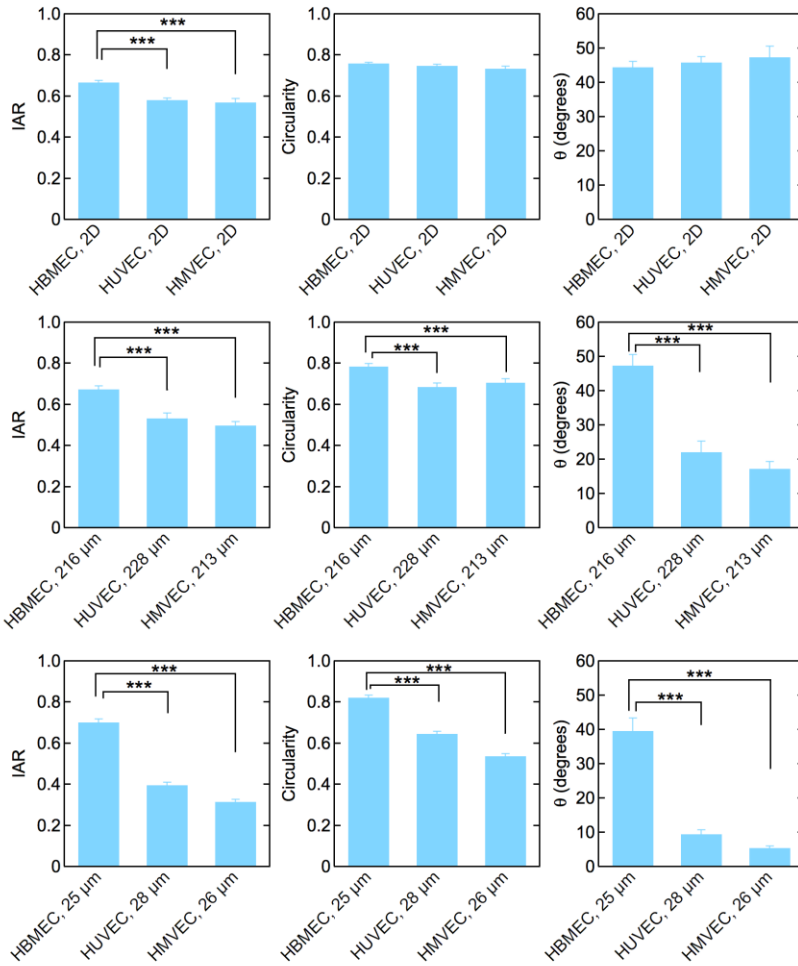
Figure 29. Cell morphological parameters for confluent monolayers of HBMEC, HUVEC and HMVECs in 2D and on large (~ 200 µm) and small (~ 20 µm) diameter glass rods.

Parameters include: inverse aspect ratio (IAR), circularity, and average orientation angle. HBMECs: 2D (N = 238), d = 216 ± 3 µm (SE) (N = 32), d = 25 ± 0 µm (N = 48).   HUVECs: 2D (N = 242), d = 228 ± 0 µm (N = 46), d = 28 ± 0 µm (N = 75).   HMVECs: 2D (N = 64), d = 213 ± 5 µm (N = 60), d = 26 ± 0 µm (N = 110).   *** P < 0.001.   Error bars represent standard error (SE).

3.3 Summary

3.3.1 Energy and cell morphology for HBMECs and HUVECs

For HBMECs the energy difference (ΔE) between the two states (axial and radial) is less than

the thermal energy (kT, where k is the Boltzmann constant and T is temperature) and hence there

is no driving force for preferential alignment. In contrast, the energy for radial orientation is larger than for axial alignment, resulting in an energy barrier for radial alignment. As a result of this energy barrier, cells tend to align along the axial direction of the rod resulting in elongation and decreased circularity, as well as a small average orientation angle. The results shown in **Figure 19** suggest that the energy barrier is dependent on curvature or rod diameter, with the energy barrier increasing with decreasing diameter.
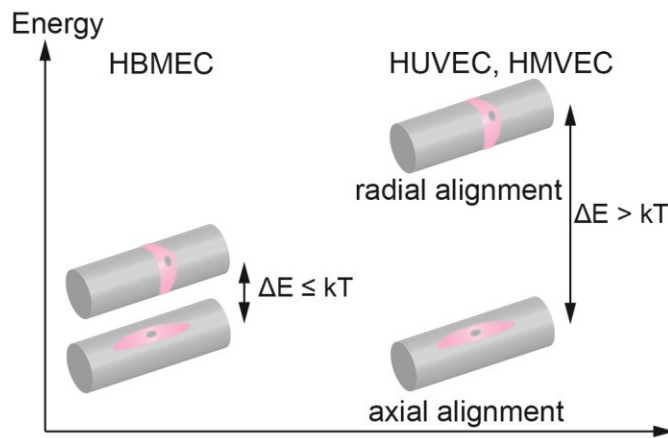
Figure 30. Schematic illustration showing the different energy states for axial and radial alignment of HBMECs, HUVECs, and HMVECs.

3.3.2 BBB permeability and junction network

There are 600 km of capillaries in brain that supply essential fuels and prevent entry of harmful chemicals, pathogens, and immune cells into the brain. The highly specialized endothelial cells that form brain capillaries are a key component of the blood-brain barrier (BBB) forming a network of tight junctions that almost completely block paracellular transport (Abbott, Patabendige et al. 2010, Daneman 2012, Wong, Ye et al. 2013). Spatially, the tight junction network that contributes to maintaining homeostasis in the brain is defined by the morphology of the endothelial cells that form the capillaries. Therefore, factors that affect cell morphology,

such as blood flow and curvature, directly influence the tight junction network. To illustrate the relationship between cell morphology and the tight junction network, we consider a simple model (**Figure 31**) where cells of fixed area are tiled onto a cylinder of fixed vessel diameter. Cells are assumed to be hexagonal in shape and aligned in the axial direction. This model illustrates that the length of tight junctions per unit length of vessel decreases with decreasing elongation (IAR).

The paracellular flux of a solute (per unit length of capillary) into the brain is determined by the permeability (per unit length of tight junction) and the length of tight junctions (per unit length of capillary). Therefore to minimize brain penetration there is an advantage to minimizing the permeability and/or the length of tight junctions per unit length of capillary. In the brain, the permeability term is minimized by forming specialized tight junctions. To minimize the length of tight junctions (per unit length of capillary), brain microvascular endothelial cells should not elongate in response to the high curvature associated with small capillaries or shear stress associated with blood flow. The results from our rod assay suggest that brain microvascular endothelial cells are programmed to resist elongation in response to curvature and shear stress, and provide support for the hypothesis that this phenotype may have evolved to minimize the length of tight junctions per unit length of capillary and hence minimize paracellular transport into the brain.
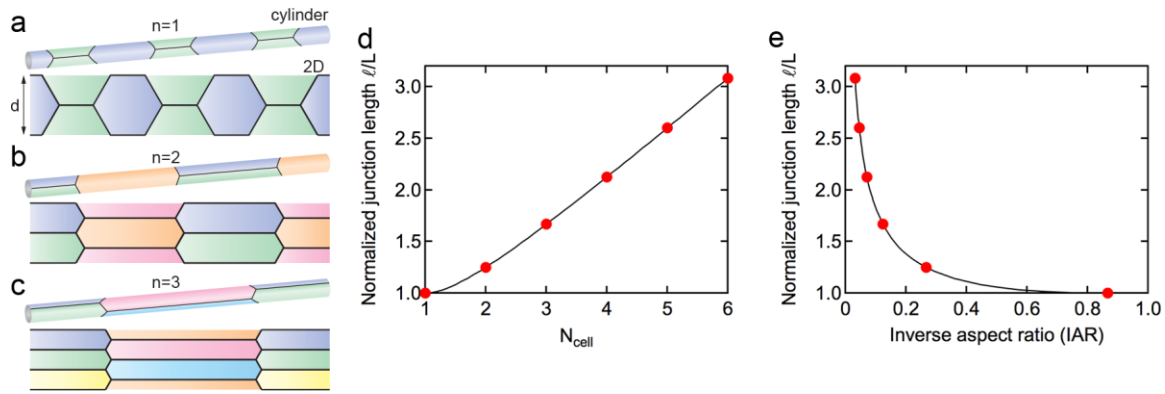
Figure 31. Relationship between cell morphology and tight junction length.

(a-c) Illustrations of junction networks for 1, 2, and 3 cells around the perimeter of a cylinder with fixed diameter. The cell shape is assumed to be hexagonal (regular or irregular) with constant area and aligned in the axial direction. (d) Normalized junction length per unit length of cylinder versus number of cells around the perimeter. (e) Normalized junction length versus the inverse aspect ratio (assuming all cells are aligned in the axial direction). Note that the inverse aspect ratio for a regular hexagon is 0.87.

Chapter 4 Conclusions and Future Directions

Modern life sciences have been revolutionized by large scale, quantitative experiments and sophisticated theoretical analyses. Numerous emerging scientific problems from fundamental research to public health are so complex that they require experts from different fields. This dissertation mainly focuses on two topics at the interface of physical and biological sciences.

4.1 Blinking in Quantum Dots

Quantum dots have attracted researchers from a broad range of interests ranging from fundamental mechanisms to various applications. Achieving a detailed understanding of fundamental mechanisms is crucial in realizing various applications. By utilizing a kinetic Monte Carlo method, this research work builds a physics framework that explains various kinds of optical behaviors of QDs. Within this framework, ensemble average parameters such as quantum yield, absorption and emission spectra can be described in a consistent way with individual parameters such as on-time fraction, power-law statistics. This research work suggests that incoming excitation light (generation rate g) can play an important role in blinking behavior, which is consistent with later experimental observations (Saba, Aresti et al. 2012).

4.2 Endothelial Cells under Curvature and Shear Stress

Cell culture is an essential tool in modern life sciences including drug discovery, tissue engineering, and stem cell research. In conventional tissue culture procedures, cells have been grown on a 2D plane. 2D cell growth may produce different gene expression, signaling and morphology from in vivo conditions, and therefore may compromise its clinical relevance (Cukierman, Pankov et al. 2001, Abbott 2003, Griffith and Swartz 2006, Atala 2007, Pampaloni,

Reynaud et al. 2007).   This research work reports a 3D tissue culture based on growing endothelial cells on the surface of glass rods.   By developing novel fluorescence microscopy techniques and image processing tools, our work enables us to quantify cell morphology on 3D cylindrical surfaces and study the curvature dependence.   By approximating the cell shapes with hexagons, we used a simple model to describe the relationship between cell morphology and junctional network.   We advocate that resistance to elongation of brain microvascular endothelial cells can yield an evolutionary advantage that helps maintain the barrier property.

Future directions include the influence of curvature and shear stress on other cell behaviors such as permeability and cell signaling, and the response of cell morphology to curvature in vivo.

Appendix I UNWRAP User Document

This MATLAB application takes a set of confocal microscope z-stack images of fluorescently labeled cells in a 3D cylindrical geometry and creates an unwrapped 2D image from the "tube" surface (**Figure 18**).   The application works best for a confluent monolayer of cells on a cylindrical surface.   The application can accommodate up to three channels (e.g. R, G, B), for example a junctional protein, a cytoskeleton protein, and a nuclear stain.   This code has been tested for MATLAB R2013b in Windows 7.

To make best use of this tutorial, download the folder "UNWRAP" from the Searson Group website (http://www.jhu.edu/searson/).   In the working folder "UNWRAP", there are two sample image folders ("images1" and "images2") and the application MATLAB file (UNWRAP.m), see **Figure A1**.   The MATLAB script (UNWRAP.m) can also be generated by copying the code from this document (see MATLAB Code).   The sample images include a confocal z-stack image of cells on a complete cylinder ("images1") and on a partial cylinder ("images2").
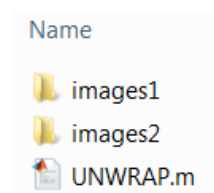
Figure A1.   Contents in the working folder "UNWRAP".

Instructions

Step 1.   For the purpose of the tutorial, the sample image folder "images1" is used as the input for "UNWRAP".   To analyze your own images, create your own image folder (e.g. "imagesX") inside the working folder, then create a sub-folder (e.g. "z_stack") inside your image folder, transfer the z-stack images for your cylindrical structure from the software associated with the confocal microscope into your sub-folder (e.g. "z_stack").   The z-stack images should be stored properly according to the following specifications (see **Step 4**):   (1) the z-stack images should be named sequentially as "common filename" + "numbers" + ".format" (e.g. "all_" + "001" + ".tif", the numbers should have the same number of digits), (2) the cylindrical structure should be vertically oriented on the screen (important for the program to handle images properly).   An example of a z-stack image near the middle of the cylinder from the folder "images1" is shown in **Figure A2.**
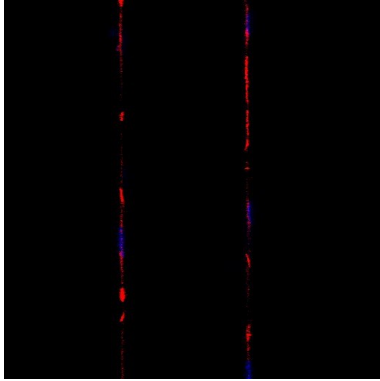
Figure A2.   An example of a z-stack image near the middle of the cylinder oriented vertically on the screen.

Step 2.   In windows, use Notepad to create a text file (.txt) inside your image folder (e.g. "imagesX") with name "scale.txt" and enter two numbers (separated by a carriage return): the first is the xy resolution (in units of μm/pixel) of each z-stack image, and second one is the spacing (in units of μm) between z-stack images (**Figure A3**).   Make sure the resolution information is saved correctly, otherwise you may get a distorted 3-D image in the following steps.   The hierarchy of your folder and files should be similar to the sample image folder "images1" or "images2" (i.e. a "scale.txt" file and a sub-folder of the image sequence inside your image folder).

```
0.41
0.2
```

Figure A3.   The resolution information stored in file "scale.txt".

In this example, 0.41 represents the xy resolution (0.41 μm/pixel), and 0.2 represents the spacing between z-stack images (0.2 μm).

Step 3.   Open UNWRAP.m in MATLB (can simply double click the file, or open it through the MATLAB "file" tab in the top left corner), then left click run ▷.   After running UNWRAP.m, a series of prompts will appear in the command window (**Figure A4**).   Enter the relevant information after each prompt and press enter.   Caution: you should type names that match exactly with your folder and file names; otherwise, program will fail.   **Figure A5** shows an example of the screen for the sample image folder "images1".   In case of a problem, press "Ctrl" + "C" in the Command Window and restart the program by clicking ▷.

```
>> UNWRAP
input the folder name (e.g. images1): images1
input the sub-folder name for z_stack images (e.g. z_stack): z_stack
input the format for z_stack images (e.g. tif): tif
input the common filename of z_stack images (e.g. all_): all_
input the number of digits in the name of each z_stack image (e.g. 3 for all_000.tif, 2 for all_00.tif): 3
input the start number for the image sequence (e.g. 0 for all_000.tif, 1 for all_001.tif): 1
```

Figure A4. Prompts appeared in the command window for sample image folder "images1". Names that need to be typed in for sample image folder "images1" are in red boxes.

Step 4. A sequence of numbers will appear in the Command Window while the program is reading all the input z-stack images and scale information from your image folder ("images1"). In about 30 seconds, a cross-section image will be displayed for the user to locate the user-defined focal plane. This is the first of two cross-section images (one at each end of the cylinder) that are used to define the focal plane of the cylinder for unwrapping. The second cross-section image will appear in **Step 7**. If your resolution information is correct and the z-stack images are stored properly (see **Step 1** and **Step 2**), you will get a circular cross-section image (**Figure A5**).
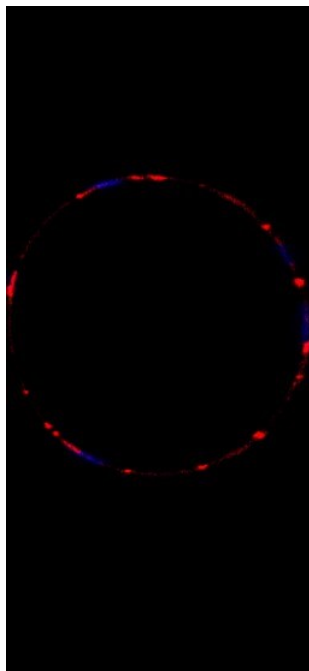
Figure A5. A cross section image of the cylindrical structure is shown on the screen.

Step 5. Create a rectangular region of interest (ROI) around the cross-section by moving your cursor to the top-left side of your circular cross-section image and holding your mouse and dragging to the bottom-right (**Figure A6**). The rectangular region of interest (ROI) MUST include the image circle. If you are not satisfied with your initial ROI, adjust the rectangle by clicking the edge of it and dragging such that it contains the whole cross section of interest with

70

an additional margin.   Double left click inside the rectangle and a zoomed-in image will be generated (**Figure A6** and **Figure A7**).
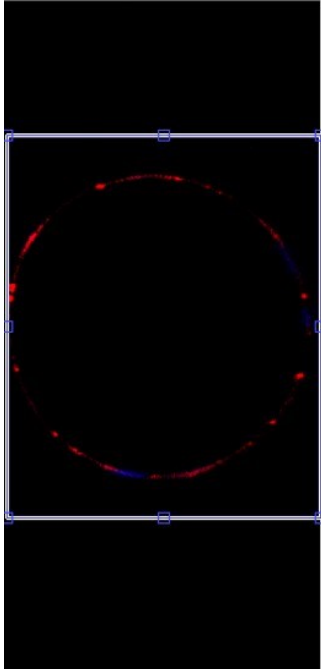
Figure A6.   A region of interest (ROI) of the cross section is created for the cylindrical structure.

slice y = 100
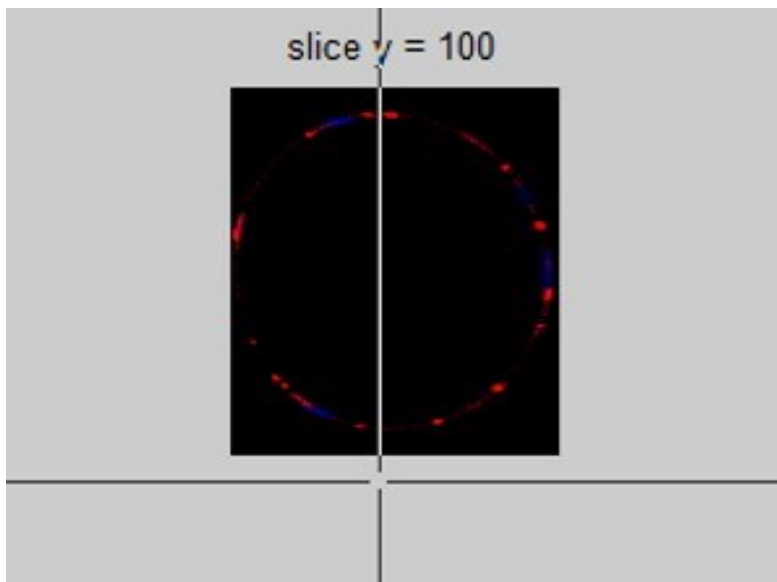
Figure A7.   A zoomed-in figure of the cross section image is generated according to a user selected region of interest.

Step 6.   Maximize the zoomed-in image (**Figure A8**) and left click 10-20 points uniformly distributed on the circular cross-section (**Figure A9**).   After each click, you will see a green cross "x" in the clicked position in the image.   If you want to change points, simply start over from **Step 3**.   After finishing selecting points, right click on the image.   A yellow fitted circle will be generated based on the input points you selected (**Figure A10**). This circle will be used as the first reference for unwrapping the cylindrical structure.
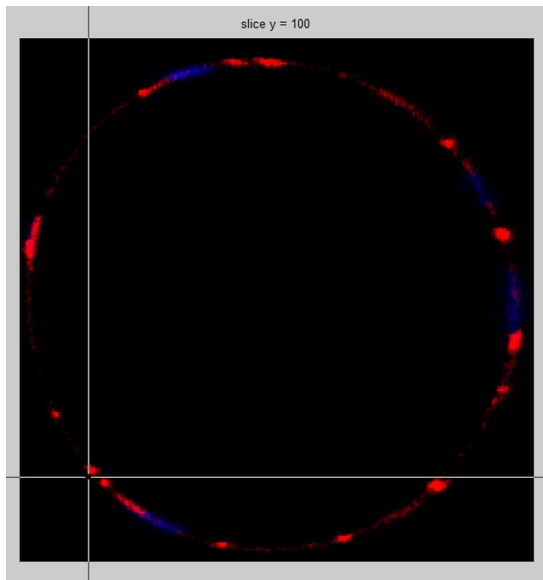
Figure A8.   The zoomed-in figure is maximized for convenient point-clicking.
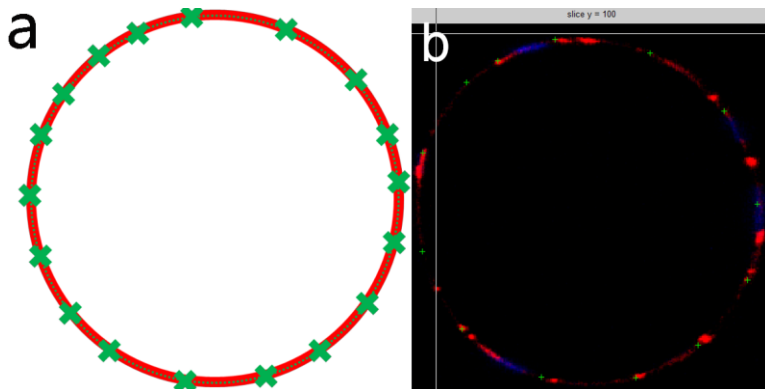
Figure A9.   Input positions from user in defining the cross section.   (a) Green "x" markers represent the positions the user should click to identify the cross section.   (b)   Green "+" markers are displayed on the screen as the user is clicking positions.

72
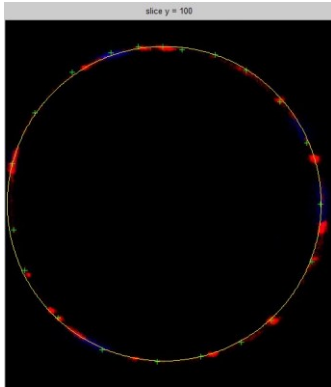
Figure A10.   A yellow fitted circle is shown as an overlay.

Step 7.   Repeat **Step 6** for the second cross section image.

Step 8.   An unwrapped image of all channels (i.e. R, G, B) will appear on the screen as your result (**Figure A11**).   In the meantime, a sub-folder called "unwrapped_images" (**Figure A12**) and an "info.txt" file (

Figure A13) will be generated inside your image folder (e.g. "images1"). Inside the "unwrapped_images" folder, the unwrapped images are separated into different combinations of channels (RGB, RB, GB, B with 1 image alone, and 2 images side-by-side).   The "info.txt" file will provide information regarding your cylinder including resolution (µm/pixel), cylinder diameter (µm), and cylinder length (µm).
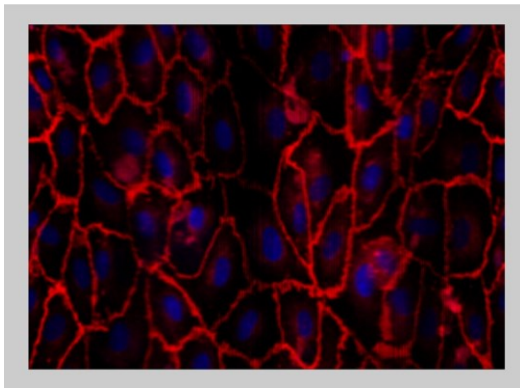
Figure A11.   An unwrapped image of the cylindrical structure is shown on the screen. This image is also saved in the output folder "unwrapped_images".

Figure A12. All unwrapped images are stored in the "unwrapped_images" folder.

```
um per pixel: 0.410000 cylinder diameter: 92.377985 cyliner length: 209.920000
```

Figure A13. Information for your input cylindrical structure, including the resolution (0.41 µm/pixel), cylinder diameter (92.4 µm), the length of the cylinder in axial direction (209.9 µm).

General Instructions

To apply this program to another image set, simply create a folder with the image sequence and "scale.txt" file in the same structure as described above, into the working folder (folder names can be different). For example, a practice image folder named "images2" is provided in the working folder. In the example in the "images2" folder, the z-stack represents only part of the cross section of a cylinder. In this case, the points selected to define the cross section should only be located on the section of the cylinder that is imaged. The information you need for this input folder is provided below (**Figure A14**).

```
>> UNWRAP
input the folder name (e.g. images1): images2
input the sub-folder name for z_stack images (e.g. z_stack): z_stack
input the format for z_stack images (e.g. tif): tif
input the common filename of z_stack images (e.g. all_): all_
input the number of digits in the name of each z_stack image (e.g. 3 for all_000.tif, 2 for all_00.tif): 2
input the start number for the image sequence (e.g. 0 for all_000.tif, 1 for all_001.tif): 1
```

Figure A14. Prompts in the command window for the sample image folder "images2". Input data is indicated by the red boxes.

For sample images, if something goes wrong, simply start over to **Step 3** by clicking ▷. For your own input images, if something goes wrong, check your folder carefully according to **Step 1** and **Step 2**.

Appendix II MATLAB Code for UNWRAP

```
% UNWRAP
%
% Mao Ye, Zhen Yang, and Peter C. Searson
% Johns Hopkins University
%
% UNWRAP takes a series of z-stack images of a cylindrical object and unwraps
% the image to create a set of 2D images for quantitative analysis.
% The original images can contain up to three separate channels.  This
% application is useful for unwrapping images of cylindrical objects such
% as small blood vessels.
%
% The main steps in the applications are:
% • Specify data folder, image format and scale info
% • Input a series of z-stack images (up to three channels)
% • Isotropic resample of the 3D volume
% • Crop the volume to focus on the cylinder
% • Fit to a cylinder
% • Unwrap the image on the surface of the cylinder to obtain a set of 2D images
% • Save unwrapped images and info

function UNWRAP()
%% Specify data folder, image format and scale info
s1 = input('input the folder name (e.g. images1): ','s');
SubjFolder = [s1, '/'];

s2 = input('input the sub-folder name for z_stack images (e.g. z_stack): ','s');
ImgFolder = [SubjFolder s2, '/'];

s3 = input('input the format for z_stack images (e.g. tif): ','s');
ImgFmt = s3; % format of input z-stack images

s4 = input('input the common filename of z_stack images (e.g. all_): ','s');
filename = s4; % common name of input images, CHANGE if filename is different!

s6 = input('input the number of digits in the name of each z_stack image (e.g.
3 for all_000.tif, 2 for all_00.tif): ','s');
digit = ['%0', s6, 'd'];% number of digits contained in names of input images,
CHANGE if number of digits is different!

s7 = input('input the start number for the image sequence (e.g. 0 for all_000.tif,
1 for all_001.tif): ','s');
start = 1; % if 0, name starts from "all_000.tif"; if 1, start from "all_001.tif",
CHANGE if the start number is different!


imageNames = dir(fullfile(ImgFolder,'images','*.tif'));
imageNames = {imageNames.name}';


% information for picking two slices in y-direction (perpendicular to cylinder)
slice_show1 = 100; % slice numberfrom one end (no need to change)
```

```matlab
slice_show2 = 100; % slice number from the other end (no need to change)

% create a result folder if there's none
RsltFolder = [SubjFolder 'unwrapped_images/'];
if ~exist(RsltFolder); mkdir(SubjFolder, 'unwrapped_images'); end


ImgName = [ImgFolder '*.' ImgFmt];
d = dir(ImgName);
SliceNos = 1 : (length(d));
SliceNum = length(SliceNos);

%image scale information
A = load([SubjFolder 'scale.txt']); % first row: xy resolution (µm/px); second
row: z-spacing between z-stack images (µm)
yScale = A(1);
zScale = A(2);
zRatio = zScale/yScale;  % z resolution / xy resolution um/px

%% Input a series of z-stack images (up to three channels)
% read one z-stack image to get the image size
s = 1;
FileName = [ImgFolder filename sprintf(digit, s) '.' ImgFmt];
Img = imread(FileName);
[Ny,Nx,Nc] = size(Img);

% prepare 3D volume for 3 channels (RGB)
RVol = zeros(Ny,Nx,SliceNum);
GVol = zeros(Ny,Nx,SliceNum);
BVol = zeros(Ny,Nx,SliceNum);

% load z-stack images of a cylindrical 3D object
display('read in slices. z = : ')
for i = 1: SliceNum
    s = start + SliceNos(i) - 1;
    fprintf('%d\t', s)
    if mod(s,5)==4
        fprintf('\r')
    end
    FileName = [ImgFolder filename sprintf(digit, s) '.' ImgFmt];
    %display(s);
    RGBImg = imread(FileName);
    RVol(:,:,i) = RGBImg(:,:,1);
    GVol(:,:,i) = RGBImg(:,:,2);
    BVol(:,:,i) = RGBImg(:,:,3);
end
fprintf('\r\r')

% normalize the image intensity to [0 1]
RVol = double(RVol)/256;
GVol = double(GVol)/256;
BVol = double(BVol)/256;
[Ny, Nx, Nz0] = size(RVol);

%% Isotropic resample of the 3D volume
```

```matlab
Nz = round(Nz0*zRatio); % target dimension in z-direction after isotropic
resampling
% prepare empty isotropic 3D volumes
IsoRVol = zeros(Ny,Nx,Nz);
IsoGVol = zeros(Ny,Nx,Nz);
IsoBVol = zeros(Ny,Nx,Nz);

% resize slice by slice in y direction
display('generate isotropic volume. y = : ')
for i = 1 : Ny
    fprintf('%d\t', i)
    if mod(i,5)==4
        fprintf('\r')
    end
    % R channel
    I = squeeze(RVol(i,:,:));
    I = imresize(I,[Nx,Nz], 'bicubic');
    IsoRVol(i,:,:) = I;
    % G channel
    I = squeeze(GVol(i,:,:));
    I = imresize(I,[Nx,Nz], 'bicubic');
    IsoGVol(i,:,:) = I;
    % B channel
    I = squeeze(BVol(i,:,:));
    I = imresize(I,[Nx,Nz], 'bicubic');
    IsoBVol(i,:,:) = I;
end
fprintf('\r\r')

%% Crop the volume to focus on the cylinder
display('crop image')
y = slice_show1; % pick a slice in y-direction

hf = figure;
% create the color image for the slice for better visualization
I = cat(3, squeeze(IsoRVol(y,:,:)), ...
        squeeze(IsoGVol(y,:,:)), ...
        squeeze(IsoBVol(y,:,:)));
[X,Y,I2,rect] = imcrop(I);

% record the cropped rectangle
zmin = rect(1);
zmax = rect(1) + rect(3);
xmin = rect(2);
xmax = rect(2) + rect(4);

% convert to positive integer
zmin = max(1, floor(zmin));
zmax = min(Nz, ceil(zmax));
xmin = max(1, floor(xmin));
xmax = min(Nx, ceil(xmax));

% crop the 3d volume according to the rectangle
IsoRVol = IsoRVol(:, xmin:xmax, zmin:zmax);
IsoGVol = IsoGVol(:, xmin:xmax, zmin:zmax);
IsoBVol = IsoBVol(:, xmin:xmax, zmin:zmax);
```

```
[Ny,Nx,Nz] = size(IsoRVol);

%% Fit to a cylinder

LEFT = 1; MIDDLE = 2; RIGHT = 3;
t = 0:pi/360:2*pi;

display('fit circle on one end')
y = slice_show1; % pick a slice near one end of the cylinder

hf = figure;
% create the color image for the slice for better visualization
I = cat(3, squeeze(IsoRVol(y,:,:)), ...
           squeeze(IsoGVol(y,:,:)), ...
           squeeze(IsoBVol(y,:,:)));
imshow(I, 'initialmagnification',50)
title(['slice y = ' num2str(y)])
hold on
P = [];
% pick points
[x,y,Button] = ginput(1);
while(Button == LEFT)
    P = [P; [x y]];
    plot(x, y, 'g+');
    [x,y,Button] = ginput(1);
end
% fit circle
% call the Circle Fit (Taubin method) from MatLab File Exchange
CirPar = FUN_CircleFitByTaubin(P);
% plot fitted circle
X = CirPar(1) + CirPar(3)*cos(t);
Y = CirPar(2) + CirPar(3)*sin(t);
plot(X,Y,'y')
hold off
% record the parameters for the first circle
CirPar1 = CirPar;

display('fit circle on the other end')
y = Ny-slice_show2; % pick a slice near the other end of the cylinder

figure;
% create the color image for the slice for better visualization
I = cat(3, squeeze(IsoRVol(y,:,:)), ...
           squeeze(IsoGVol(y,:,:)), ...
           squeeze(IsoBVol(y,:,:)));
imshow(I)
title(['slice y = ' num2str(y)])
hold on
P = [];
% pick points
[x,y,Button] = ginput(1);
while(Button == LEFT)
    P = [P; [x y]];
    plot(x, y, 'g+');
```

78

```
    [x,y,Button] = ginput(1);
end
% fit circle
CirPar = FUN_CircleFitByTaubin(P);
% plot fitted circle
X = CirPar(1) + CirPar(3)*cos(t);
Y = CirPar(2) + CirPar(3)*sin(t);
plot(X,Y,'y')
hold off
% record the parameters for the second circle
CirPar2 = CirPar;

% average the parameters of the two circles
CirPar = (CirPar1 + CirPar2)/2;

%% Unwrap the image on the surface of the cylinder to obtain a set of 2D images

Rc = CirPar(3); % radius of the cylinder in the image
% number of angles to sample around the cylinder axis
dTheta = 1/Rc;
MinTheta = 0;
MaxTheta = 2*pi-dTheta;
Theta = MinTheta : dTheta : MaxTheta;
ThetaNum = length(Theta);

% number of sample points along cylinder axis
dHeight = dTheta*Rc;
MinHeight = 1;
MaxHeight = Ny;
Height = MinHeight : dHeight : MaxHeight;
HeightNum = length(Height);

Rot = eye(3);
t0 = [CirPar(2)  0  CirPar(1)]';

% smoothing parameter
r = 2; %2
s = (2*r+1)^3;
sigma = 1;

% prepare empty unwrap images for three channels
IsoRGrid = zeros(HeightNum, ThetaNum);
IsoGGrid = zeros(HeightNum, ThetaNum);
IsoBGrid = zeros(HeightNum, ThetaNum);

XX = zeros(HeightNum, ThetaNum);
YY = zeros(HeightNum, ThetaNum);
ZZ = zeros(HeightNum, ThetaNum);

for it = 1 : ThetaNum % sample around cylinder axis
    theta = Theta(it);
    for ih = 1 : HeightNum % sample along cylinder axis
        % compute the spatial coordinate of sample point p0
        height = Height(ih);
        p0 = [Rc*sin(theta)
```

```matlab
            height
            Rc*cos(theta)];
        p0 = Rot*p0 + t0;
        p0 = round(p0);
        x0 = p0(1); y0 = p0(2); z0 = p0(3);

        XX(ih,it) = x0;
        YY(ih,it) = y0;
        ZZ(ih,it) = z0;

        % coordinate span of p0's neighborhood
        xspan = max(x0-r,1):min(x0+r,Nx);
        yspan = max(y0-r,1):min(y0+r,Ny);
        zspan = max(z0-r,1):min(z0+r,Nz);

        if isempty(xspan)||isempty(yspan)||isempty(zspan)
            IsoRGrid(ih,it) = 0;
            IsoGGrid(ih,it) = 0;
            IsoBGrid(ih,it) = 0;
        end

        % average pixel intensity in p0's neighborhood and assign to the
        % correponding pixel in the unswrapped image
        I = IsoRVol(yspan, xspan, zspan);
        IsoRGrid(ih,it) = sum(I(:))/s;
        I = IsoGVol(yspan, xspan, zspan);
        IsoGGrid(ih,it) = sum(I(:))/s;
        I = IsoBVol(yspan, xspan, zspan);
        IsoBGrid(ih,it) = sum(I(:))/s;
    end
end

%% Save unwrapped images and info
RGBGrid1 = cat(3,IsoRGrid, IsoGGrid, IsoBGrid);
RGBGrid2 = cat(3,repmat(IsoRGrid,1,2), ...
    repmat(IsoGGrid,1,2), ...
    repmat(IsoBGrid,1,2));

RGBGrid3 = cat(3,zeros(size(IsoRGrid)), zeros(size(IsoGGrid)), IsoBGrid);
RGBGrid4 = cat(3,repmat(zeros(size(IsoRGrid)),1,2), ...
    repmat(zeros(size(IsoGGrid)),1,2), ...
    repmat(IsoBGrid,1,2));

RGBGrid5 = cat(3,IsoRGrid, zeros(size(IsoRGrid)), IsoBGrid);
RGBGrid6 = cat(3,repmat(IsoRGrid,1,2), ...
    repmat(zeros(size(IsoRGrid)),1,2), ...
    repmat(IsoBGrid,1,2));

RGBGrid7 = cat(3,zeros(size(IsoRGrid)), IsoGGrid, IsoBGrid);
RGBGrid8 = cat(3,repmat(zeros(size(IsoRGrid)),1,2), ...
    repmat(IsoGGrid,1,2), ...
    repmat(IsoBGrid,1,2));

figure
imshow(RGBGrid1)
```

```matlab
axis image

% save unwrapped images
imwrite(RGBGrid1, [RsltFolder 'unwrap1.png'], 'png');
imwrite(RGBGrid2, [RsltFolder 'unwrap2.png'], 'png');
imwrite(RGBGrid3, [RsltFolder 'unwrap_blue1.png'], 'png');
imwrite(RGBGrid4, [RsltFolder 'unwrap_blue2.png'], 'png');

imwrite(RGBGrid5, [RsltFolder 'unwrap_rb1.png'], 'png');
imwrite(RGBGrid6, [RsltFolder 'unwrap_rb2.png'], 'png');
imwrite(RGBGrid7, [RsltFolder 'unwrap_gb1.png'], 'png');
imwrite(RGBGrid8, [RsltFolder 'unwrap_gb2.png'], 'png');

% save unwrap info
fid = fopen([SubjFolder 'info.txt'], 'w');
fprintf(fid, 'um per pixel: %f \n', yScale);
fprintf(fid, 'cylinder diameter: %f \n', 2*Rc*yScale);
fprintf(fid, 'cyliner length: %f \n', Ny*yScale);
fclose(fid);


end



% The following session is obtained from MATLAB file exchange.
%
http://www.mathworks.com/matlabcentral/fileexchange/22678-circle-fit-taubin-m
ethod


function Par = FUN_CircleFitByTaubin(XY)

%--------------------------------------------------------------------------
%
%     Circle fit by Taubin
%      G. Taubin, "Estimation Of Planar Curves, Surfaces And Nonplanar
%                Space Curves Defined By Implicit Equations, With
%                Applications To Edge And Range Image Segmentation",
%      IEEE Trans. PAMI, Vol. 13, pages 1115-1138, (1991)
%
%     Input:  XY(n,2) is the array of coordinates of n points x(i)=XY(i,1),
y(i)=XY(i,2)
%
%     Output: Par = [a b R] is the fitting circle:
%                     center (a,b) and radius R
%
%     Note: this fit does not use built-in matrix functions (except "mean"),
%           so it can be easily programmed in any programming language
%
%--------------------------------------------------------------------------

n = size(XY,1);      % number of data points

centroid = mean(XY);   % the centroid of the data set
```

```
%    computing moments (note: all moments will be normed, i.e. divided by n)

Mxx = 0; Myy = 0; Mxy = 0; Mxz = 0; Myz = 0; Mzz = 0;

for i=1:n
    Xi = XY(i,1) - centroid(1);  % centering data
    Yi = XY(i,2) - centroid(2);  % centering data
    Zi = Xi*Xi + Yi*Yi;
    Mxy = Mxy + Xi*Yi;
    Mxx = Mxx + Xi*Xi;
    Myy = Myy + Yi*Yi;
    Mxz = Mxz + Xi*Zi;
    Myz = Myz + Yi*Zi;
    Mzz = Mzz + Zi*Zi;
end

Mxx = Mxx/n;
Myy = Myy/n;
Mxy = Mxy/n;
Mxz = Mxz/n;
Myz = Myz/n;
Mzz = Mzz/n;

%    computing the coefficients of the characteristic polynomial

Mz = Mxx + Myy;
Cov_xy = Mxx*Myy - Mxy*Mxy;
A3 = 4*Mz;
A2 = -3*Mz*Mz - Mzz;
A1 = Mzz*Mz + 4*Cov_xy*Mz - Mxz*Mxz - Myz*Myz - Mz*Mz*Mz;
A0 = Mxz*Mxz*Myy + Myz*Myz*Mxx - Mzz*Cov_xy - 2*Mxz*Myz*Mxy + Mz*Mz*Cov_xy;
A22 = A2 + A2;
A33 = A3 + A3 + A3;

xnew = 0;
ynew = 1e+20;
epsilon = 1e-12;
IterMax = 20;

% Newton's method starting at x=0

for iter=1:IterMax
    yold = ynew;
    ynew = A0 + xnew*(A1 + xnew*(A2 + xnew*A3));
    if abs(ynew) > abs(yold)
       disp('Newton-Taubin goes wrong direction: |ynew| > |yold|');
       xnew = 0;
       break;
    end
    Dy = A1 + xnew*(A22 + xnew*A33);
    xold = xnew;
    xnew = xold - ynew/Dy;
    if (abs((xnew-xold)/xnew) < epsilon), break, end
    if (iter >= IterMax)
```

```
            disp('Newton-Taubin will not converge');
            xnew = 0;
        end
        if (xnew<0.)
            fprintf(1,'Newton-Taubin negative root:  x=%f\n',xnew);
            xnew = 0;
        end
end

%  computing the circle parameters

DET = xnew*xnew - xnew*Mz + Cov_xy;
Center = [Mxz*(Myy-xnew)-Myz*Mxy , Myz*(Mxx-xnew)-Mxz*Mxy]/DET/2;

Par = [Center+centroid , sqrt(Center*Center'+Mz)];

end   %   CircleFitByTaubin
```

Bibliography

Abbott, A. (2003). "Cell culture: Biology's new dimension." <u>Nature</u> **424**(6951): 870-872.

Abbott, N. J., A. A. K. Patabendige, D. E. M. Dolman, S. R. Yusof and D. J. Begley (2010). "Structure and function of the blood–brain barrier." <u>Neurobiology of Disease</u> **37**(1): 13-25.

Abbott, N. J., L. Ronnback and E. Hansson (2006). "Astrocyte-endothelial interactions at the blood-brain barrier." <u>Nat Rev Neurosci</u> **7**(1): 41-53.

Aird, W. C. (2005). "Spatial and temporal dynamics of the endothelium." <u>Journal of Thrombosis and Haemostasis</u> **3**(7): 1392-1406.

Aird, W. C. (2007). "Phenotypic Heterogeneity of the Endothelium: I. Structure, Function, and Mechanisms." <u>Circulation Research</u> **100**(2): 158-173.

Aird, W. C. (2007). "Phenotypic Heterogeneity of the Endothelium: II. Representative Vascular Beds." <u>Circulation Research</u> **100**(2): 174-190.

Alivisatos, A. P. (1996). "Semiconductor Clusters, Nanocrystals, and Quantum Dots." <u>Science</u> **271**(5251): 933-937.

Atala, A. (2007). "Engineering tissues, organs and cells." <u>Journal of Tissue Engineering and Regenerative Medicine</u> **1**(2): 83-96.

Bazzoni, G. and E. Dejana (2004). <u>Endothelial Cell-to-Cell Junctions: Molecular Organization and Role in Vascular Homeostasis</u>.

Blatt, R. and P. Zoller (1988). "Quantum jumps in atomic systems." <u>European Journal of Physics</u> **9**(4): 250.

Bohr, N. (1915). "XLII. On the Quantum theory of radiation and the structure of the atom." <u>The London, Edinburgh, and Dublin Philosophical Magazine and Journal of Science</u> **30**(177): 394-415.

Bout, D. A. V., W.-T. Yip, D. Hu, D.-K. Fu, T. M. Swager and P. F. Barbara (1997). "Discrete Intensity Jumps and Intramolecular Electronic Energy Transfer in the Spectroscopy of Single Conjugated Polymer Molecules." <u>Science</u> **277**(5329): 1074-1077.

Brightman, M. W. (1977). "Morphology of blood-brain interfaces." <u>Experimental Eye Research</u> **25, 1**(0): 1-25.

Brus, L. (1986). "Electronic wave functions in semiconductor clusters: experiment and theory." <u>The Journal of Physical Chemistry</u> **90**(12): 2555-2560.

Chien, S. (2007). <u>Mechanotransduction and endothelial cell homeostasis: the wisdom of the cell</u>.

Chung, I. and M. G. Bawendi (2004). "Relationship between single quantum-dot intermittency and fluorescence intensity decays from collections of dots." Physical Review B **70**(16): 165304.

Cichos, F., C. von Borczyskowski and M. Orrit (2007). "Power-law intermittency of single emitters." Current Opinion in Colloid & Interface Science **12**(6): 272-284.

Cook, R. J. and H. J. Kimble (1985). "Possibility of Direct Observation of Quantum Jumps." Physical Review Letters **54**(10): 1023-1026.

Crooker, S. A., J. A. Hollingsworth, S. Tretiak and V. I. Klimov (2002). "Spectrally Resolved Dynamics of Energy Transfer in Quantum-Dot Assemblies: Towards Engineered Energy Flows in Artificial Materials." Physical Review Letters **89**(18): 186802.

Crouch, C. H., O. Sauter, X. Wu, R. Purcell, C. Querner, M. Drndic and M. Pelton (2010). "Facts and Artifacts in the Blinking Statistics of Semiconductor Nanocrystals." Nano Letters **10**(5): 1692-1698.

Cucullo, L., M. Hossain, V. Puvenna, N. Marchi and D. Janigro (2011). "The role of shear stress in Blood-Brain Barrier endothelial physiology." BMC Neuroscience **12**(1): 40.

Cukierman, E., R. Pankov, D. R. Stevens and K. M. Yamada (2001). "Taking Cell-Matrix Adhesions to the Third Dimension." Science **294**(5547): 1708-1712.

Curtis, A. S. G. and M. Varde (1964). "Control of Cell Behavior: Topological Factors." Journal of the National Cancer Institute **33**(1): 15-26.

Daneman, R. (2012). "The blood–brain barrier in health and disease." Annals of Neurology **72**(5): 648-672.

Daniel, C. and A. S. Martin (2012). "Lessons from the endothelial junctional mechanosensory complex." F1000 Biology Reports **4**.

Davies, P. F. (1995). Flow-mediated endothelial mechanotransduction.

Dejana, E. (2004). "Endothelial cell-cell junctions: happy together." Nat Rev Mol Cell Biol **5**(4): 261-270.

Dickson, R. M., A. B. Cubitt, R. Y. Tsien and W. E. Moerner (1997). "On/off blinking and switching behaviour of single molecules of green fluorescent protein." Nature **388**(6640): 355-358.

Dolan, J., J. Kolega and H. Meng (2013). "High Wall Shear Stress and Spatial Gradients in Vascular Pathology: A Review." Annals of Biomedical Engineering **41**(7): 1411-1427.

Dunn, G. A. and J. P. Heath (1976). "A new hypothesis of contact guidance in tissue cells." Experimental Cell Research **101**(1): 1-14.

Efros, A. L. and M. Rosen (1997). "Random Telegraph Signal in the Photoluminescence Intensity of a Single Quantum Dot." Physical Review Letters **78**(6): 1110-1113.

Eigenmann, D., G. Xue, K. Kim, A. Moses, M. Hamburger and M. Oufir (2013). "Comparative study of four immortalized human brain capillary endothelial cell lines, hCMEC/D3, hBMEC, TY10, and BB19, and optimization of culture conditions, for an in vitro blood-brain barrier model for drug permeability studies." Fluids and Barriers of the CNS **10**(1): 33.

Ekimov, A. and A. Onushchenko (1981). "Quantum size effect in three-dimensional microscopic semiconductor crystals." ZhETF Pisma Redaktsiiu **34**: 363.

Eskin, S. G., C. L. Ives, L. V. McIntire and L. T. Navarro (1984). "Response of cultured endothelial cells to steady flow." Microvascular Research **28**(1): 87-94.

Fernando, D. S., Z. Xinhua, K. Wolfgang, H. Mingyong and K. Maximilian (2005). "Memory in quantum-dot photoluminescence blinking." New Journal of Physics **7**(1): 197.

Fichthorn, K. A. and W. H. Weinberg (1991). "Theoretical foundations of dynamical Monte Carlo simulations." The Journal of Chemical Physics **95**(2): 1090-1096.

Fisher, B. R., H.-J. Eisler, N. E. Stott and M. G. Bawendi (2003). "Emission Intensity Dependence and Single-Exponential Behavior In Single Colloidal Quantum Dot Fluorescence Lifetimes." The Journal of Physical Chemistry B **108**(1): 143-148.

Fisher, P. E. and C. Tickle (1981). "Differences in alignment of normal and transformed cells on glass fibres." Experimental Cell Research **131**(2): 407-410.

Fomenko, V. and D. J. Nesbitt (2007). "Solution Control of Radiative and Nonradiative Lifetimes: A Novel Contribution to Quantum Dot Blinking Suppression." Nano Letters **8**(1): 287-293.

Franke, R. P., M. Grafe, H. Schnittler, D. Seiffge, C. Mittermayer and D. Drenckhahn (1984). "Induction of human vascular endothelial stress fibres by fluid shear stress." Nature **307**(5952): 648-649.

Frantsuzov, P., M. Kuno, B. Janko and R. A. Marcus (2008). "Universal emission intermittency in quantum dots, nanorods and nanowires." Nat Phys **4**(5): 519-522.

Frantsuzov, P. A. and R. A. Marcus (2005). "Explanation of quantum dot blinking without the long-lived trap hypothesis." Physical Review B **72**(15): 155321.

Furuse, M. and S. Tsukita (2006). "Claudins in occluding junctions of humans and flies." Trends in Cell Biology **16**(4): 181-188.

Gao, X., Y. Cui, R. M. Levenson, L. W. K. Chung and S. Nie (2004). "In vivo cancer targeting and imaging with semiconductor quantum dots." Nat Biotech **22**(8): 969-976.

Glennon, J. J., R. Tang, W. E. Buhro and R. A. Loomis (2007). "Synchronous Photoluminescence Intermittency (Blinking) along Whole Semiconductor Quantum Wires." Nano Letters **7**(11): 3290-3295.

Gómez, D. E., J. van Embden, P. Mulvaney, M. J. Fernée and H. Rubinsztein-Dunlop (2009). "Exciton−Trion Transitions in Single CdSe–CdS Core–Shell Nanocrystals." ACS Nano **3**(8): 2281-2287.

Goushi, K., T. Yamada and A. Otomo (2009). "Excitation Intensity Dependence of Power-Law Blinking Statistics in Nanocrystal Quantum Dots." The Journal of Physical Chemistry C **113**(47): 20161-20168.

Griffith, L. G. and M. A. Swartz (2006). "Capturing complex 3D tissue physiology in vitro." Nat Rev Mol Cell Biol **7**(3): 211-224.

Gupta, T. K. and J. Doh (1992). "Optical properties of polycrystalline CdSe films." Journal of Materials Research **7**(05): 1243-1246.

Haase, M., C. G. Hübner, E. Reuther, A. Herrmann, K. Müllen and T. Basché (2004). "Exponential and Power-Law Kinetics in Single-Molecule Fluorescence Intermittency†." The Journal of Physical Chemistry B **108**(29): 10445-10450.

Hahn, C. and M. A. Schwartz (2009). "Mechanotransduction in vascular physiology and atherogenesis." Nat Rev Mol Cell Biol **10**(1): 53-62.

Haug, A. (1983). "Auger recombination in direct-gap semiconductors: band-structure effects." Journal of Physics C: Solid State Physics **16**(21): 4159.

Hawkins, B. T. and T. P. Davis (2005). "The Blood-Brain Barrier/Neurovascular Unit in Health and Disease." Pharmacological Reviews **57**(2): 173-185.

Hohng, S. and T. Ha (2004). "Near-Complete Suppression of Quantum Dot Blinking in Ambient Conditions." Journal of the American Chemical Society **126**(5): 1324-1325.

Hoogenboom, J. P., J. Hernando, E. M. H. P. van Dijk, N. F. van Hulst and M. F. García-Parajó (2007). "Power-Law Blinking in the Fluorescence of Single Organic Molecules." ChemPhysChem **8**(6): 823-833.

Hoogenboom, J. P., E. M. H. P. van Dijk, J. Hernando, N. F. van Hulst and M. F. García-Parajó (2005). "Power-Law-Distributed Dark States are the Main Pathway for Photobleaching of Single Organic Molecules." Physical Review Letters **95**(9): 097401.

Htoon, H., A. V. Malko, D. Bussian, J. Vela, Y. Chen, J. A. Hollingsworth and V. I. Klimov (2010). "Highly Emissive Multiexcitons in Steady-State Photoluminescence of Individual "Giant" CdSe/CdS Core/Shell Nanocrystals." Nano Letters **10**(7): 2401-2407.

Huynh, W. U., X. Peng and A. P. Alivisatos (1999). "CdSe Nanocrystal Rods/Poly(3-hexylthiophene) Composite Photovoltaic Devices." Advanced Materials **11**(11): 923-927.

Jha, P. P. and P. Guyot-Sionnest (2009). "Trion Decay in Colloidal Quantum Dots." ACS Nano **3**(4): 1011-1015.

Johnson, B. D., K. J. Mather and J. P. Wallace (2011). "Mechanotransduction of shear in the endothelium: Basic studies and clinical implications." Vascular Medicine **16**(5): 365-377.

Kairdolf, B. A., A. M. Smith, T. H. Stokes, M. D. Wang, A. N. Young and S. Nie (2013). "Semiconductor Quantum Dots for Bioimaging and Biodiagnostic Applications." Annual Review of Analytical Chemistry **6**(1): 143-162.

Kamiya, A., R. Bukhari and T. Togawa (1984). "Adaptive regulation of wall shear stress optimizing vascular tree function." Bulletin of Mathematical Biology **46**(1): 127-137.

Klimov, V. I., A. A. Mikhailovsky, D. W. McBranch, C. A. Leatherdale and M. G. Bawendi (2000). "Quantization of Multiparticle Auger Rates in Semiconductor Quantum Dots." Science **287**(5455): 1011-1013.

Knappenberger, K. L., D. B. Wong, W. Xu, A. M. Schwartzberg, A. Wolcott, J. Z. Zhang and S. R. Leone (2008). "Excitation-Wavelength Dependence of Fluorescence Intermittency in CdSe Nanorods." ACS Nano **2**(10): 2143-2153.

Koutsiaris, A. G., S. V. Tachmitzi, N. Batis, M. G. Kotoula, C. H. Karabatsas, E. Tsironi and D. Z. Chatzoulis (2007). "Volume flow and wall shear stress quantification in the human conjunctival capillaries and post-capillary venules in vivo." Biorheology **44**(5): 375-386.

Kramer, I. J. and E. H. Sargent (2013). "The Architecture of Colloidal Quantum Dot Solar Cells: Materials to Devices." Chemical Reviews **114**(1): 863-882.

Kraus, R. M., P. G. Lagoudakis, J. Müller, A. L. Rogach, J. M. Lupton, J. Feldmann, D. V. Talapin and H. Weller (2005). "Interplay between Auger and Ionization Processes in Nanocrystal Quantum Dots." The Journal of Physical Chemistry B **109**(39): 18214-18217.

Krauss, T. D. and J. J. Peterson (2010). "Bright Future for Fluorescence Blinking in Semiconductor Nanocrystals." The Journal of Physical Chemistry Letters **1**(9): 1377-1382.

Krizanac-Bengez, L., M. R. Mayberg and D. Janigro (2004). "The cerebral vasculature as a therapeutic target for neurological disorders and the role of shear stress in vascular homeostatis and pathophysiology." Neurological Research **26**(8): 846-853.

Kuno, M., D. P. Fromm, H. F. Hamann, A. Gallagher and D. J. Nesbitt (2000). "Nonexponential "blinking" kinetics of single CdSe quantum dots: A universal power law behavior." The Journal of Chemical Physics **112**(7): 3117-3120.

Kuno, M., D. P. Fromm, H. F. Hamann, A. Gallagher and D. J. Nesbitt (2001). ""On"/"off" fluorescence intermittency of single semiconductor quantum dots." The Journal of Chemical Physics **115**(2): 1028-1040.

Kuno, M., D. P. Fromm, S. T. Johnson, A. Gallagher and D. J. Nesbitt (2003). "Modeling distributed kinetics in isolated semiconductor quantum dots." Physical Review B **67**(12): 125304.

Landsberg, P. T. (1970). "Non-Radiative Transitions in Semiconductors." physica status solidi (b) **41**(2): 457-489.

Lee, E. S., K. Na and Y. H. Bae (2003). "Polymeric micelle for tumor pH and folate-mediated targeting." Journal of Controlled Release **91**(1–2): 103-113.

Levesque, M. J. and R. M. Nerem (1985). "The Elongation and Orientation of Cultured Endothelial Cells in Response to Shear Stress." Journal of Biomechanical Engineering **107**(4): 341-347.

Levina, E. M., L. V. Domnina, Y. A. Rovensky and J. M. Vasiliev (1996). "Cylindrical Substratum Induces Different Patterns of Actin Microfilament Bundles in Nontransformed and in ras-Transformed Epitheliocytes." Experimental Cell Research **229**(1): 159-165.

Liu, Z., W. Cai, L. He, N. Nakayama, K. Chen, X. Sun, X. Chen and H. Dai (2007). "In vivo biodistribution and highly efficient tumour targeting of carbon nanotubes in mice." Nat Nano **2**(1): 47-52.

Mahler, B., P. Spinicelli, S. Buil, X. Quelin, J.-P. Hermier and B. Dubertret (2008). "Towards non-blinking colloidal quantum dots." Nat Mater **7**(8): 659-664.

Malek, A. M. and S. Izumo (1996). "Mechanism of endothelial cell shape change and cytoskeletal remodeling in response to fluid shear stress." Journal of Cell Science **109**(4): 713-726.

Margolin, G. and E. Barkai (2004). "Aging correlation functions for blinking nanocrystals, and other on–off stochastic processes." The Journal of Chemical Physics **121**(3): 1566-1577.

Mattoussi, H., L. H. Radzilowski, B. O. Dabbousi, E. L. Thomas, M. G. Bawendi and M. F. Rubner (1998). "Electroluminescence from heterostructures of poly(phenylene vinylene) and inorganic CdSe nanocrystals." Journal of Applied Physics **83**(12): 7965-7974.

Michler, P., A. Imamoglu, M. D. Mason, P. J. Carson, G. F. Strouse and S. K. Buratto (2000). "Quantum correlation among photons from a single quantum dot at room temperature." Nature **406**(6799): 968-970.

Nagourney, W., G. Janik and H. Dehmelt (1983). "Linewidth of single laser-cooled 24Mg+ ion in radiofrequency trap." Proceedings of the National Academy of Sciences **80**(2): 643-646.

Nerem, R. M., M. J. Levesque and J. F. Cornhill (1981). "Vascular Endothelial Morphology as an Indicator of the Pattern of Blood Flow." Journal of Biomechanical Engineering **103**(3): 172-176.

Neuhauser, R. G., K. T. Shimizu, W. K. Woo, S. A. Empedocles and M. G. Bawendi (2000). "Correlation between Fluorescence Intermittency and Spectral Diffusion in Single Semiconductor Quantum Dots." Physical Review Letters **85**(15): 3301-3304.

Neuhauser, W., M. Hohenstatt, P. Toschek and H. Dehmelt (1978). "Optical-Sideband Cooling of Visible Atom Cloud Confined in Parabolic Well." Physical Review Letters **41**(4): 233-236.

Neuwelt, E., N. J. Abbott, L. Abrey, W. A. Banks, B. Blakley, T. Davis, B. Engelhardt, P. Grammas, M. Nedergaard, J. Nutt, W. Pardridge, G. A. Rosenberg, Q. Smith and L. R. Drewes (2008). "Strategies to advance translational research into brain barriers." The Lancet Neurology **7**(1): 84-96.

Neuwelt, E. A., B. Bauer, C. Fahlke, G. Fricker, C. Iadecola, D. Janigro, L. Leybaert, Z. Molnár, M. E. O'Donnell, J. T. Povlishock, N. R. Saunders, F. Sharp, D. Stanimirovic, R. J. Watts and L. R. Drewes (2011). "Engaging neuroscience to advance translational research in brain barrier biology." Nat Rev Neurosci **12**(3): 169-182.

Nirmal, M., B. O. Dabbousi, M. G. Bawendi, J. J. Macklin, J. K. Trautman, T. D. Harris and L. E. Brus (1996). "Fluorescence intermittency in single cadmium selenide nanocrystals." Nature **383**(6603): 802-804.

Nitta, T., M. Hata, S. Gotoh, Y. Seo, H. Sasaki, N. Hashimoto, M. Furuse and S. Tsukita (2003). "Size-selective loosening of the blood-brain barrier in claudin-5–deficient mice." The Journal of Cell Biology **161**(3): 653-660.

Nizet, V., K. S. Kim, M. Stins, M. Jonas, E. Y. Chi, D. Nguyen and C. E. Rubens (1997). "Invasion of brain microvascular endothelial cells by group B streptococci." Infection and Immunity **65**(12): 5074-5081.

Nozik, A. J., M. C. Beard, J. M. Luther, M. Law, R. J. Ellingson and J. C. Johnson (2010). "Semiconductor Quantum Dots and Quantum Dot Arrays and Applications of Multiple Exciton Generation to Third-Generation Photovoltaic Solar Cells." Chemical Reviews **110**(11): 6873-6890.

Pampaloni, F., E. G. Reynaud and E. H. K. Stelzer (2007). "The third dimension bridges the gap between cell culture and live tissue." Nat Rev Mol Cell Biol **8**(10): 839-845.

Papaioannou, T. G. and C. Stefanadis (2005). "Vascular wall shear stress: basic principles and methods." Hellenic J Cardiol **46**(1): 9-15.

Pelton, M., D. G. Grier and P. Guyot-Sionnest (2004). "Characterizing quantum-dot blinking using noise power spectra." Applied Physics Letters **85**(5): 819-821.

Peterson, J. J. and D. J. Nesbitt (2008). "Modified Power Law Behavior in Quantum Dot Blinking: A Novel Role for Biexcitons and Auger Ionization." Nano Letters **9**(1): 338-345.

Protasenko, V., S. Gordeyev and M. Kuno (2007). "Spatial and Intensity Modulation of Nanowire Emission Induced by Mobile Charges." Journal of the American Chemical Society **129**(43): 13160-13171.

Protasenko, V. V., K. L. Hull and M. Kuno (2005). "Disorder-Induced Optical Heterogeneity in Single CdSe Nanowires." Advanced Materials **17**(24): 2942-2949.

Reese, T. S. and M. J. Karnovsky (1967). "FINE STRUCTURAL LOCALIZATION OF A BLOOD-BRAIN BARRIER TO EXOGENOUS PEROXIDASE." The Journal of Cell Biology **34**(1): 207-217.

Reidy, M. A. and B. Lowell Langille (1980). "The effect of local blood flow patterns on endothelial cell morphology." Experimental and Molecular Pathology **32**(3): 276-289.

Rovensky, Y. and V. I. Samoilov (1994). "Morphogenetic response of cultured normal and transformed fibroblasts, and epitheliocytes, to a cylindrical substratum surface. Possible role for the actin filament bundle pattern." Journal of Cell Science **107**(5): 1255-1263.

Roy, S., A. Aguirre, D. A. Higgins and V. Chikan (2011). "Investigation of Charge Transfer Interactions in CdSe Nanorod P3HT/PMMA Blends by Optical Microscopy." The Journal of Physical Chemistry C **116**(4): 3153-3160.

Saba, M., M. Aresti, F. Quochi, M. Marceddu, M. A. Loi, J. Huang, D. V. Talapin, A. Mura and G. Bongiovanni (2012). "Light-Induced Charged and Trap States in Colloidal Nanocrystals Detected by Variable Pulse Rate Photoluminescence Spectroscopy." ACS Nano **7**(1): 229-238.

Sauter, T., W. Neuhauser, R. Blatt and P. E. Toschek (1986). "Observation of Quantum Jumps." Physical Review Letters **57**(14): 1696-1698.

Schlegel, G., J. Bohnenberger, I. Potapova and A. Mews (2002). "Fluorescence Decay Time of Single Semiconductor Nanocrystals." Physical Review Letters **88**(13): 137401.

Shimizu, K. T., R. G. Neuhauser, C. A. Leatherdale, S. A. Empedocles, W. K. Woo and M. G. Bawendi (2001). "Blinking statistics in single semiconductor nanocrystal quantum dots." Physical Review B **63**(20): 205316.

Shockley, W. and W. T. Read (1952). "Statistics of the Recombinations of Holes and Electrons." Physical Review **87**(5): 835-842.

Silkworth, J. B., W. E. Stehbens and D. Phil (1975). "The Shape of Endothelial Cells in En Face Preparations of Rabbit Blood Vessels." Angiology **26**(6): 474-487.

Simmers, M. B., A. W. Pryor and B. R. Blackman (2007). Arterial shear stress regulates endothelial cell-directed migration, polarity, and morphology in confluent monolayers.

Spinicelli, P., S. Buil, X. Quélin, B. Mahler, B. Dubertret and J. P. Hermier (2009). "Bright and Grey States in CdSe-CdS Nanocrystals Exhibiting Strongly Reduced Blinking." Physical Review Letters **102**(13): 136801.

Stefani, F. D., J. P. Hoogenboom and E. Barkai (2009). "Beyond quantum jumps: blinking nanoscale light emitters." Phys. Today **62**(2): 34-39.

Stins, M. F., N. V. Prasadarao, J. Zhou, M. Arditi and K. S. Kim (1997). "Bovine Brain Microvascular Endothelial Cells Transfected with SV40-Large T Antigen: Development of an Immortalized Cell Line to Study Pathophysiology of CNS Disease." In Vitro Cellular & Developmental Biology. Animal **33**(4): 243-247.

Svitkina, T. M., Y. A. Rovensky, A. D. Bershadsky and J. M. Vasiliev (1995). "Transverse pattern of microfilament bundles induced in epitheliocytes by cylindrical substrata." Journal of Cell Science **108**(2): 735-745.

Tang, J. and R. A. Marcus (2005). "Diffusion-Controlled Electron Transfer Processes and Power-Law Statistics of Fluorescence Intermittency of Nanoparticles." Physical Review Letters **95**(10): 107401.

Tarbell, J. M. (2010). "Shear stress and the endothelial transport barrier." Cardiovascular Research **87**(2): 320-330.

Trindade, T., P. O'Brien and N. L. Pickett (2001). "Nanocrystalline Semiconductors: Synthesis, Properties, and Perspectives." Chemistry of Materials **13**(11): 3843-3858.

Turitto, V. (1982). "Blood viscosity, mass transport, and thrombogenesis." Progress in hemostasis and thrombosis **6**: 139.

Verberk, R., A. M. van Oijen and M. Orrit (2002). "Simple model for the power-law blinking of single semiconductor nanocrystals." Physical Review B **66**(23): 233202.

Wang, L.-W., M. Califano, A. Zunger and A. Franceschetti (2003). "Pseudopotential Theory of Auger Processes in CdSe Quantum Dots." Physical Review Letters **91**(5): 056404.

Wang, S., C. Querner, T. Emmons, M. Drndic and C. H. Crouch (2006). "Fluorescence Blinking Statistics from CdSe Core and Core/Shell Nanorods." The Journal of Physical Chemistry B **110**(46): 23221-23227.

Wang, X., X. Ren, K. Kahen, M. A. Hahn, M. Rajeswaran, S. Maccagnano-Zacher, J. Silcox, G. E. Cragg, A. L. Efros and T. D. Krauss (2009). "Non-blinking semiconductor nanocrystals." Nature **459**(7247): 686-689.

Weissleder, R., K. Kelly, E. Y. Sun, T. Shtatland and L. Josephson (2005). "Cell-specific targeting of nanoparticles by multivalent attachment of small molecules." Nat Biotech **23**(11): 1418-1423.

Wong, A., M. Ye, A. Levy, J. Rothstein, D. Bergles and P. C. Searson (2013). "The Blood-Brain Barrier: An Engineering Perspective." <u>Frontiers in Neuroengineering</u> **6**.

Wustholz, K. L., E. D. Bott, C. M. Isborn, X. Li, B. Kahr and P. J. Reid (2007). "Dispersive Kinetics from Single Molecules Oriented in Single Crystals of Potassium Acid Phthalate." <u>The Journal of Physical Chemistry C</u> **111**(26): 9146-9156.

Yeow, E. K. L., S. M. Melnikov, T. D. M. Bell, F. C. De Schryver and J. Hofkens (2006). "Characterizing the Fluorescence Intermittency and Photobleaching Kinetics of Dye Molecules Immobilized on a Glass Surface." <u>The Journal of Physical Chemistry A</u> **110**(5): 1726-1734.

Zhang, K., H. Chang, A. Fu, A. P. Alivisatos and H. Yang (2006). "Continuous Distribution of Emission States from Single CdSe/ZnS Quantum Dots." <u>Nano Letters</u> **6**(4): 843-847.

Zhao, J., G. Nair, B. R. Fisher and M. G. Bawendi (2010). "Challenge to the Charging Model of Semiconductor-Nanocrystal Fluorescence Intermittency from Off-State Quantum Yields and Multiexciton Blinking." <u>Physical Review Letters</u> **104**(15): 157403.

Vita

Mao Ye was born in Xiaogan, Hubei, China. He received his undergraduate education in University of Science and Technology of China where he majored in Physics. He came to Johns Hopkins University in 2009 to pursue graduate study in the Henry A. Rowland Department of Physics and Astronomy. He has worked with Professor Peter Searson since 2010. He obtained his M.A. degree in Physics in 2012 and M.S.E. degree in Applied Mathematics and Statistics in 2014.